



## Full Length Article



# Phosphorus encapsulated gallium nitride and aluminum nitride nanotubes as nonenzymatic sensors for fructose, glucose, and xylose sugars as biomarkers for diabetes-mellitus: Outlook from computational study

Anna Imojara<sup>a</sup>, Joyce E. Ishegbe<sup>b</sup>, Hewa Abdullah<sup>g</sup>, Henry O. Edet<sup>a</sup>, Terkumbur E. Gber<sup>a,c,\*</sup>, Maxwell-Borjor A. Eba<sup>e</sup>, Anthony M.S. Pembere<sup>f</sup>, Hitler Louis<sup>a,c,d,\*</sup>

<sup>a</sup> Computational and Bio-Simulation Research Group, University of Calabar, Calabar, Nigeria

<sup>b</sup> Department of Chemistry, Bingham University, Karu, Nigeria

<sup>c</sup> Department of Pure and Applied Chemistry, University of Calabar, Calabar, Nigeria

<sup>d</sup> Centre for Herbal Pharmacology and Environmental Sustainability, Chettinad Hospital and Research Institute, Chettinad Academy of Research and Education, Kelambakkam, Tamil Nadu 603103, India

<sup>e</sup> Department of History and International Studies, University of Calabar, Nigeria

<sup>f</sup> Department of Chemistry, Jaramogi Odinga University of Science and Technology, Kenya

<sup>g</sup> Physics Education Department, Faculty of Education, Tishk International University, Erbil, Kurdistan Region 44001, Iraq

## ARTICLE INFO

**Keywords:**  
Sugar detection  
Nanotubes  
Doping  
Adsorption  
Density functional theory (DFT)

## ABSTRACT

Excessive sugar consumption has been correlated with various adverse health outcomes, encompassing both short-term and long-term implications for human well-being. Traditional approaches for sugar detection, such as chromatography, spectroscopy, and enzymatic assays, necessitate significant time, specialized equipment, and expertise. In this study, we explore the potential of phosphorus-doped Gallium nitride (P@GaNNT) and aluminum nitride (P@AlNNT) nanotubes as novel means to detect three distinct sugars: fructose (F), glucose (G), and xylose (X). To investigate their capabilities, we employ density functional theory (DFT) computations at the B3LYP-D3(BJ)/def2-SVP methodology. The molecular orbital analysis of the complexes provided evidence of reduced energy gap (Eg) values compared to the surfaces in their pristine states. The X\_P@AlNNT interaction was the most stable complex, with an energy gap (Eg) value of 4.408eV while G\_P@AlNNT was the most reactive complex, with an Eg value of 0.545eV. When these complexes were evaluated in a solvent (water), their stability was found to be higher than their reactivity, as evidenced by the increased Eg values for each complex. Results from topological studies (QTAIM and NCI) showed the presence of covalent, electrostatic, and weak van der Waals interactions among atoms in these systems. The adsorption energies for F\_P@AlNNT and F\_P@GaNNT indicated that fructose was chemisorbed onto P@AlNNT and P@GaNNT, with values of -1.442eV and -1.469eV, respectively. On the other hand, glucose and xylose were found to be physisorbed on P@GaNNT and P@AlNNT, based on the positive results from their adsorption. This study demonstrated the potential of P@AlNNT and P@GaNNT as valuable tools for sugar detection.

## 1. Introduction

Excessive sugar intake has been linked to a range of health implications, affecting both short-term and long-term well-being [1]. In the short term, excessive sugar consumption can lead to various issues, including tooth decay, primarily because sugar promotes the growth of bacteria in the mouth, which can harm tooth enamel. Additionally, it can contribute to weight gain and obesity due to its calorie content

devoid of essential nutrients [2]. Furthermore, the rapid spikes and subsequent crashes in blood sugar levels caused by high sugar intake can result in energy fluctuations and fatigue [3]. Over the long term, excessive sugar consumption is associated with more serious health conditions, such as type 2 diabetes, as it can lead to insulin resistance and reduced glucose tolerance. It also plays a role in cardiovascular diseases by contributing to elevated blood pressure, increased cholesterol levels, and chronic inflammation [4]. Another concerning

\* Corresponding authors at: Computational and Bio-Simulation Research Group, University of Calabar, Calabar, Nigeria.

E-mail addresses: [gberterkumburemanuel@gmail.com](mailto:gberterkumburemanuel@gmail.com) (T.E. Gber), [louismuzong@gmail.com](mailto:louismuzong@gmail.com) (H. Louis).

consequence is the accumulation of fat in the liver, which can progress to non-alcoholic fatty liver disease [5]. Some studies have even suggested a potential link between excessive sugar consumption and certain types of cancer, including breast and colon cancer [6]. Traditional methods for detecting sugar levels involve techniques like chromatography, spectroscopy, and enzymatic tests, but these methods are time-consuming and require specialized equipment and expertise [7].

Sugar is extensively prevalent in various industries, including medical diagnostics, the food sector, environmental monitoring, biological systems, and industrial applications [8]. It serves as a type of carbohydrate present in a wide range of foods, playing a crucial role as an energy source by supplying glucose, which is essential for cellular fuel [9]. Comprising carbon, hydrogen, and oxygen atoms, sugar falls into the category of simple carbohydrates, characterized by one or two sugar molecules [10]. These sugars are further classified into three types: monosaccharides, disaccharides, and polysaccharides [11]. Monosaccharides, such as glucose, fructose, and galactose, consist of single sugar molecules [12]. Among these, xylose, a member of the pentose group of five-carbon sugars is another example of a monosaccharide, composed of a single sugar molecule [13]. Xylose can be sourced from various plant materials like wood, straw, and corn cobs, which can be extracted and refined for utilization across multiple industries [14]. Disaccharides, including sucrose (common table sugar), lactose found in dairy products, and maltose, are formed by the bonding of two sugar molecules, and they are commonly found in grains [15]. Polysaccharides, on the other hand, are composed of numerous sugar molecules linked together, with examples like starch in grains and vegetables and cellulose in plant cell walls [16]. When consumed, sugar is broken down into its components and enters the bloodstream [17]. In response to the presence of glucose in the bloodstream, the pancreas releases insulin, a hormone that regulates blood sugar levels by facilitating glucose uptake into the body's cells [18]. While sugar is a crucial energy source, excessive consumption can have detrimental effects on health, including obesity, type 2 diabetes, heart disease, and other related concerns [19].

Nanotechnology is rapidly advancing and holds great promise in revolutionizing the field of healthcare, including detection, diagnosis, and treatment of various health issues [20]. Numerous studies have explored the application of various nanomaterials in diverse fields. For example, Marom et al. investigated the effectiveness of gold nanoparticle sensors in detecting chronic kidney disease and tracking disease progression [21]. Tisch and colleagues focused on detecting Alzheimer's and Parkinson's diseases by analyzing exhaled breath using nanomaterial-based sensors. Their findings suggested that these sensors have the potential to serve as cost-effective, rapid, and reliable biosensors for these diseases in the future [22]. Zhang et al. utilized Pd-doped  $\gamma$ -graphyne to detect dissolved gasses in transformer oil through density functional theory analysis. The research demonstrated that Pd-graphyne exhibits promising gas-sensing capabilities, particularly for CO detection, laying the groundwork for innovative nanomaterial-based gas sensors for industrial use [23]. In another study, Mohammadi and Jafari investigated the detection of food spoilage and adulteration using novel nanomaterial-based sensors. Their research indicated that these sensors could be employed in smart food packaging to meet consumer demands in the modern era [24]. Roohi and Ardehijani employed a method to investigate the adsorption behavior of NO, NO<sub>2</sub>, CO, and CS<sub>2</sub> molecules on the surface of a carbon-doped gallium nitride nanosheet. Their study revealed that the CN-GaNNS-based sensor exhibits significant potential for the detection of NO and NO<sub>2</sub>, thanks to its substantial conductance change. Moreover, it demonstrated efficient gas elimination capabilities due to its favorable adsorption energy [25]. In a separate study, Shlaka and Nasria utilized the DFT method to analyze the interaction between AsH<sub>3</sub> gas molecules and monolayer aluminum nitride (AlN) sheets, including pristine, carbon-doped, boron-doped, and defective variations. Their findings suggest that doped aluminum nitride sheets could serve as promising sensors for detecting AsH<sub>3</sub> gas molecules

[26].

Nanomaterials have demonstrated promising applications in bio-sensing, enabling the detection of essential molecules such as glucose, fructose, and xylose. These molecules play crucial roles in various biological processes, including cardiovascular health and cancer [27]. As a result, the objective of this study is to assess the applicability of phosphorus-doped AlNNT and GaNNT nanotubes in the detection of sugars, specifically fructose (F), glucose (G), and xylose (X). Phosphorus doping of AlNNT and GaNNT surfaces was employed, consistent with previous studies, to enhance the detection capabilities for these biomarkers. Our investigation of doped surfaces is presented herein, encompassing the calculation and analysis of quantum descriptors, adsorption energy, thermodynamic properties, and geometric parameters as electronic characteristics. Adsorption energy values for both the biomarkers and doped surfaces were computed utilizing the B3LYP-D3 (BJ)/def2svp method. Furthermore, the nature of interactions was determined through the quantum theory of atom in molecules (QTAIM) and non-covalent interactions (NCI).

## 2. Computational details

The DFT method was employed to perform geometric optimizations on phosphorus (P) doped Aluminum nitride nanotubes (AlNNT) and Gallium nitride nanotubes (GaNNT) for the adsorption of three different sugars: fructose (F), glucose (G), and xylose (X). Each Aluminum and Gallium nitride nanotube consisted of 100 atoms, with one nitrogen atom in each nanotube being substituted by phosphorus. All computational calculations were carried out using the Gaussian16 software package, employing the B3LYP-D3(BJ)/def2-SVP level of theory [28]. This computational approach combines the unique features of the B3LYP exchange-correlation functional with the def2-SVP basis set. The B3LYP functional blends the Becke three-parameter exchange functional with the Lee-Yang-Parr correlation functional [29], and it is well-established for producing highly accurate predictions of molecular structures, reaction energies, and other molecular characteristics [30]. Frequency calculations were also conducted at the same level of theory to confirm the absence of imaginary frequencies and ensure that the surfaces reached their potential energy minima. The strongly negative adsorption energy values obtained from these calculations underscore the robust surface adsorption of the investigated sugars [31], with the adsorption energy being determined using Eq. (1).

$$E_{ads} = E_{Complex} - (E_{Nanotube} + E_{Biomarker}) \quad (1)$$

Where:  $E_{(Complex)}$  is the total energy of the sugar molecule adsorbed on the P@AlNNT and P@GaNNT models,  $E_{(Nanotube)}$  is the energy of the nanotube models and  $E_{(Biomarkers)}$  is the energy of the sugar molecules. Higher negative adsorption energy gives rise to a shorter final adsorption distance, charge transfer, and a stronger adsorption effect [32]. Frontier molecular orbitals (FMOs) and global reactivity parameters as proposed by Koopmans which provides insights on the reactivity and kinetic stability of studied complexes were calculated for the systems using the HOMO and LUMO values and energy gap determined from the FMO analysis via the Eqs. (2) – (7)

$$E_g = E_{LUMO} - E_{HOMO} \quad (2)$$

$$\mu = \frac{HOMO + LUMO}{2} \quad (3)$$

$$\sigma = \frac{1}{2\eta} \quad (4)$$

$$\eta = \frac{HOMO - LUMO}{2} \quad (5)$$

$$\chi = -\mu = \frac{HOMO + LUMO}{2} \quad (6)$$

$$\omega = \frac{\mu^2}{2\eta} \quad (7)$$

The HOMO-LUMO plot was generated using Chemcraft software. Density of state plots for the examined complex were generated using Multiwfn analyzer and Origin to assess the impact of sugar adsorption on phosphorus-doped Aluminum nitride and Gallium nitride nanotubes [33,34]. To delve deeper into the stabilization of the studied complexes through electron exchange between donor and acceptor atoms, NBO analysis was conducted with the assistance of NBO 7.0, a component of the Gaussian software suite. For a more comprehensive understanding of both inter and intramolecular interactions between sugar molecules and nanotube surfaces, quantum theory of atoms in molecules (QTAIM) analysis was employed. Additionally, an analysis of weak interactions, such as hydrogen bonds and van der Waals interactions, was performed using the non-covalent interaction (NCI) approach. A graphical representation of the reduced density gradient (RDG) against the second eigenvalue of the electron density Hessian matrix ( $\lambda_2$ ) and the electron density  $\rho$ (a.u) was constructed and visualized using VMD software [35]. In this visualization, the blue regions indicate hydrogen bonds, the red regions signify steric effects, and the green regions represent Van der Waals interactions.

$$RDG = \frac{1}{2(3\pi^2)^{1/3}} \frac{|\Delta\rho(r)|}{\rho(r)^{1/3}} \quad (8)$$

Finally, the thermodynamic properties of examined complexes was computed with the aid of Eqs. (9)–(11), the parameters; Enthalpy, Entropy and Gibbs free energy were obtained to infer the thermodynamic favorability of complexes, either exothermic or endothermic,

spontaneous or non-spontaneous.

$$\Delta H^0(298K) = \Sigma_{product}\Delta_f H^0_{prod}(298k) - \Sigma_{reactant}\Delta_f H^0_{react}(298k) \quad (9)$$

$$\Delta_f H^0(298k) = \Sigma(E_0 + H_{corr})_{product} - \Sigma(E_0 + H_{corr})_{reactants} \quad (10)$$

$$\Delta_r G^0(298k) = \Sigma(E_0 + G_{corr})_{product} - \Sigma(E_0 + G_{corr})_{reactants} \quad (11)$$

Where  $E_0$  signifies the electronic energy of the reactant and product,  $\Delta_f H^0$  denotes the enthalpy of production of the product and reactant.  $H_{corr}$  and  $G_{corr}$  represent the sum of electronic energy (EE) and thermal correction for the product and reactant, respectively.

### 3. Results and discussion

#### 3.1. Geometric analysis

The Figs. 1 and 2 illustrate the stable geometry of the optimized models P@AlNNT and P@GaNNNT surfaces, along with the interactions involving the sugar biomarkers, namely Glucose (G), Fructose (F), and Xylose (X). Consistent with previous research, it is well-established that doping tends to enhance both sensitivity and adsorptive characteristics of nanomaterials [36,37]. Specifically, Roohi and Ardehjeni's work indicates a Ga-N bond length of 1.861Å [38,39], and our findings align closely with this, reporting a Ga-N bond length of 1.832Å. These results corroborate previous studies. Additionally, our study observes an Al-N bond length of 1.828Å, consistent with Ahmadi and colleagues' reported bond length of 1.834Å for Al-N [40,41]. It is noteworthy that these bond lengths are influenced by the nanotube's diameter,

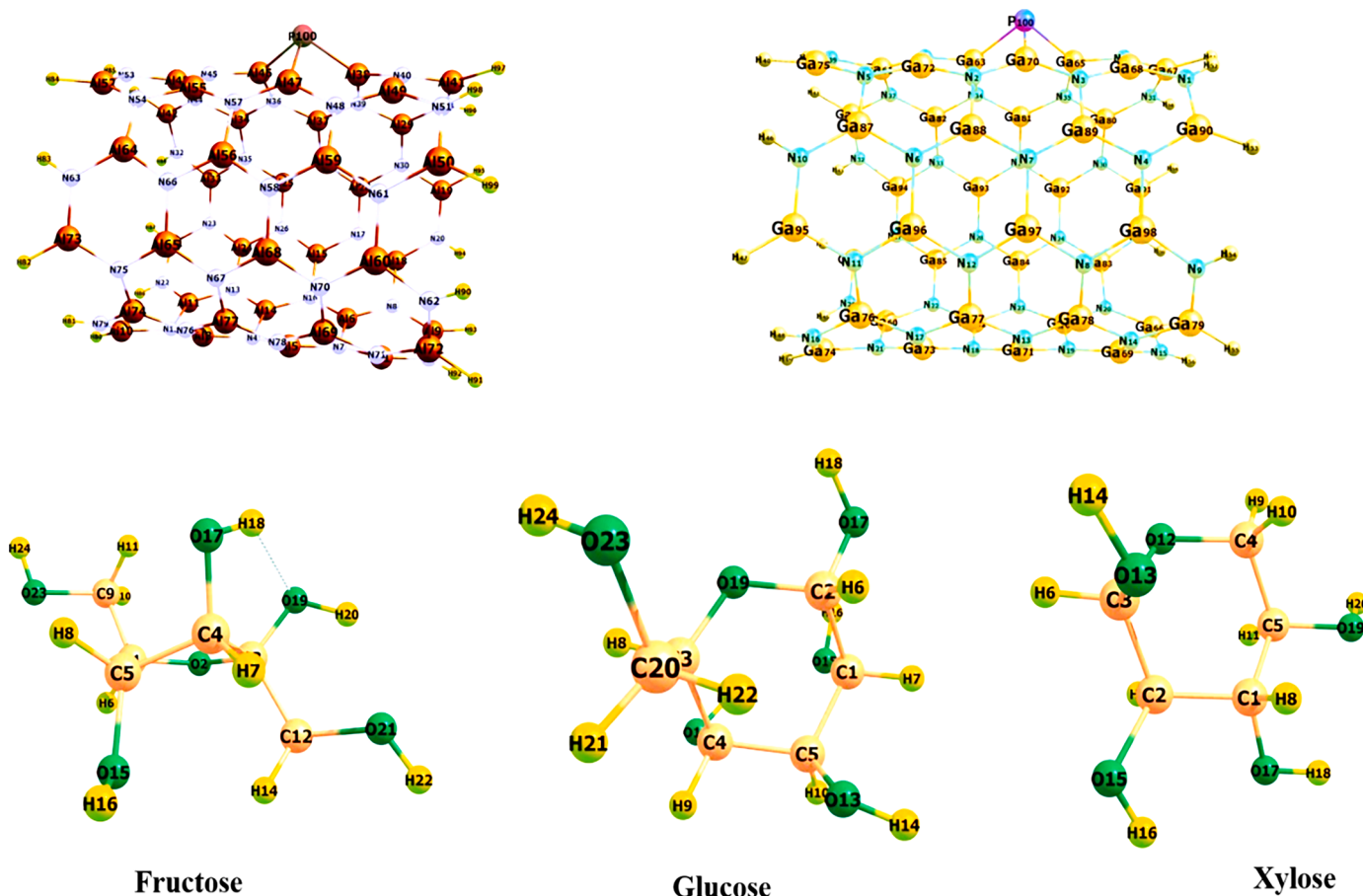


Fig. 1. Optimized structure of phosphorus doped Aluminium nitride nanotube (P@AlNNT), Gallium nitride nanotube (P@GaNNNT), fructose (F), glucose (G) and Xylose (X) optimized at the B3LYP-D3(BJ)/def2-SVP method.

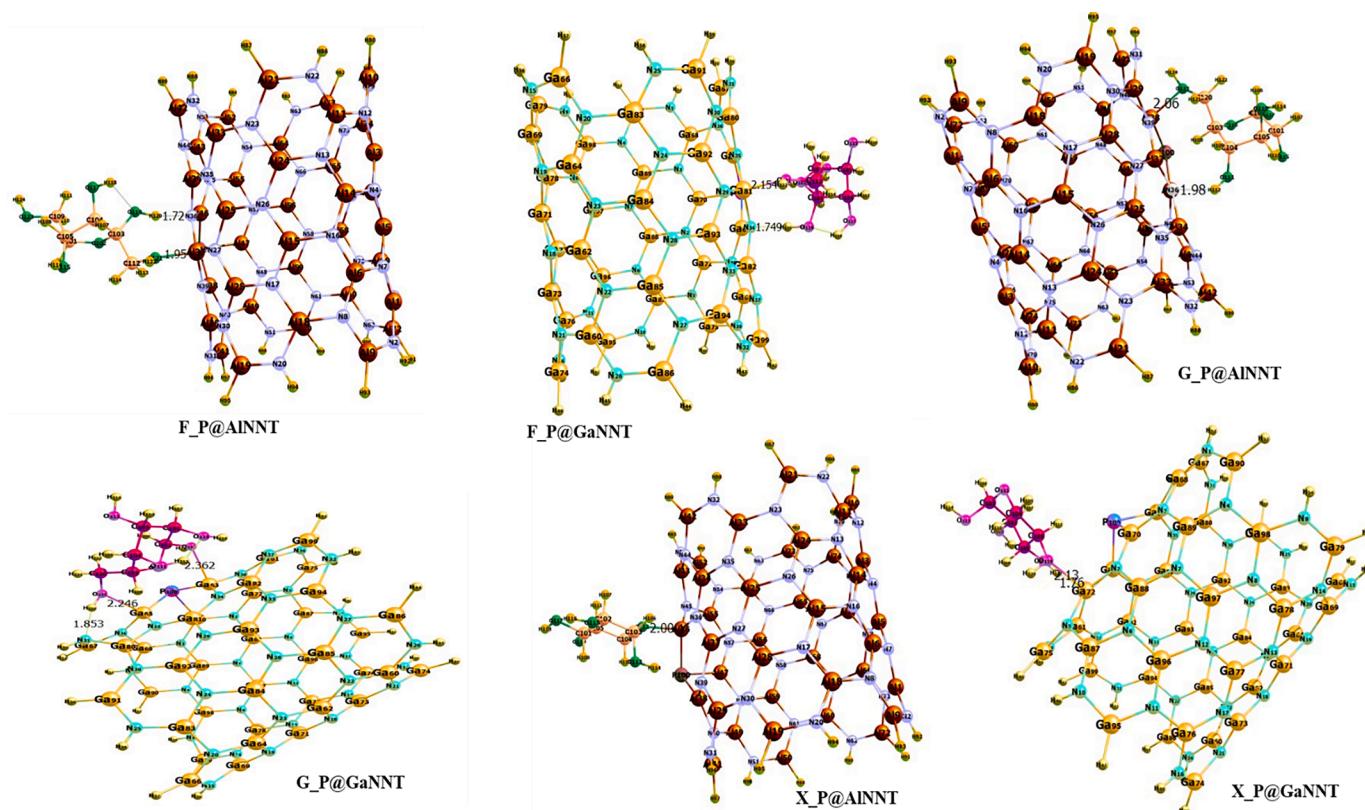


Fig. 2. Bond lengths of the interacted surfaces; F\_P@AlNNT, F\_P@GaNT, G\_P@AlNNT, G\_P@GaNT, X\_P@AlNNT and X\_P@GaNT optimized at the B3LYP-D3 (BJ)/def2-SVP method.

indicating that an increase in nanotube diameter leads to a proportional increase in bond length [42,43].

Fig. 1 shows the optimized structures of the complexes F\_P@AlNNT, F\_P@GaNT, G\_P@AlNNT, G\_P@GaNT, X\_P@AlNNT and X\_P@GaNT before and after adsorption. According to Table 1, in F\_P@AlNNT, the bond length between O<sub>121</sub> and Al<sub>37</sub> was reduced from 2.18 Å before interaction to 1.95 Å after adsorption. Similarly, the bond distance between N<sub>36</sub> of the nanotube and H<sub>120</sub> of the fructose molecule changed from 2.71 Å to 1.72 Å upon adsorption. In F\_P@GaNT, the bond length between Ga<sub>81</sub> and O<sub>121</sub> was found to be 2.68 Å and 2.15 Å before and after adsorption respectively. The shorter bond lengths observed in F\_P@AlNNT suggest that AlNNT interacts more strongly with the adsorbate than GaNT does. In G\_P@AlNNT, the bond between Al<sub>38</sub> and O<sub>123</sub> and between N<sub>36</sub> and H<sub>112</sub> were observed to be of length 2.18 Å and 3.88 Å before adsorption, respectively. After adsorption, the former was found to shorten to 2.06 Å and the latter to 1.74 Å. In

G\_P@GaNT, the O<sub>123</sub>-Ga<sub>65</sub> bond was observed to be of length 2.96 Å before adsorption and reduced to 2.24 Å after adsorption. Moreover, the bond between N<sub>31</sub> and H<sub>124</sub> changed from 3.28 Å to 1.85 Å upon adsorption. Similarly, in X\_P@AlNNT, the bond length between Al<sub>46</sub> and O<sub>112</sub> reduced from 2.43 Å to 2.00 Å after adsorption, whereas in X\_P@GaNT, the O<sub>119</sub>-Ga<sub>72</sub> bond decreased from 2.97 Å to 2.12 Å upon adsorption. Additionally, the bond between H<sub>118</sub> and N<sub>30</sub> was also shortened from 3.42 Å to 1.76 Å upon adsorption. It is evident from the results that all of the bonds observed showed a reduction in length upon adsorption, indicating that the adsorbate molecules were indeed interacting with the nanotube structures, thus confirming the formation of the complexes which is in tandem to previous findings by [44].

### 3.2. HOMO-LUMO analysis

Molecular orbitals arise from the overlapping of atomic orbitals [45] and result from the mathematical combination of functions representing these atomic orbitals [46,47]. They play a pivotal role in elucidating electronic transitions and exploring excited states within organic compounds [48]. Understanding the energies of the Highest Occupied Molecular Orbital (HOMO) and the Lowest Unoccupied Molecular Orbital (LUMO) facilitates the investigation of charge transfer reactions and the molecule's propensity to either donate or accept electrons [49]. To delve deeper into the adsorption process of fructose, glucose, and xylose onto nano-tubes, we conducted a Frontier Molecular Orbital (FMO) analysis, the results of which are presented before and after interaction. Fig. S1 illustrates the visualized molecular orbitals. Focusing on the Frontier Molecular Orbital (FMO) analysis, particular attention is given to the HOMO (representing electron donation) and the LUMO (representing electron acceptance) [50]. FMOs offer valuable insights into the system's electrical, optical, and physical properties, as well as its chemical reactivity and kinetic stability [51]. Notably, the interaction between the HOMO and LUMO, including UV-Vis spectral properties, can be

Table 1

Bond length of studied interaction before and after adsorption evaluated the B3LYP-D3(BJ)/def2-SVP level of theory.

| Systems   | Bond label                         | Bond length (Å) |           |
|-----------|------------------------------------|-----------------|-----------|
|           |                                    | Before ads      | After ads |
| F_P@AlNNT | O <sub>121</sub> -Al <sub>37</sub> | 2.18            | 1.95      |
|           | N <sub>36</sub> -H <sub>120</sub>  | 2.71            | 1.72      |
| F_P@GaNT  | Ga <sub>81</sub> -O <sub>121</sub> | 2.68            | 2.15      |
|           | N <sub>34</sub> -H <sub>120</sub>  | 2.32            | 1.74      |
| G_P@AlNNT | Al <sub>38</sub> -O <sub>123</sub> | 2.18            | 2.06      |
|           | N <sub>36</sub> -H <sub>112</sub>  | 3.88            | 1.98      |
| G_P@GaNT  | O <sub>123</sub> -Ga <sub>65</sub> | 2.96            | 2.24      |
|           | N <sub>31</sub> -H <sub>124</sub>  | 3.28            | 1.85      |
| X_P@AlNNT | Al <sub>46</sub> -O <sub>112</sub> | 2.43            | 2.00      |
| X_P@GaNT  | Ga <sub>72</sub> -O <sub>119</sub> | 2.97            | 2.12      |
|           | H <sub>118</sub> -N <sub>30</sub>  | 3.42            | 1.76      |

explained by molecular orbital theory. The shapes of these frontier molecular orbitals unveil potential positions for intra- or intermolecular interactions or reactions, as well as the spectroscopic characteristics of  $\pi$ -conjugated molecular systems [52]. The energy gap, denoted as  $E_g$  and representing the difference between HOMO and LUMO energies, serves as a critical parameter. As the system approaches a transition state, a decreasing HOMO-LUMO gap signifies various chemical events involving electron density transfer from HOMO to LUMO and implies chemical reactivity, while an increasing energy gap indicates chemical stability [53,54]. Table 2 shows that pristine P@AlNNT and P@GaNT nanotubes exhibit energy gaps of 4.654eV and 4.300eV, respectively. Similarly, Asapu et al. conducted a study on phosphorus-doped titania nanotubes, revealing that phosphorus doping decreased the band gap from 3.22eV to 2.95eV [55]. Upon the adsorption of fructose onto P@AlNNT, the energy gap decreased to 1.551eV, whereas P@GaNT exhibited a reduced energy gap of 1.230eV. When glucose interacted with P@AlNNT and P@GaNT, energy gaps of 0.545eV and 0.699eV were observed, respectively. Conversely, xylose demonstrated a distinct trend when interacting with P@AlNNT and P@GaNT, with energy gaps of 4.408eV and 4.299eV, respectively. Based on the energy gap analysis, both surfaces investigated effectively detect these sugars in the gas phase. However, they exhibit greater efficiency in detecting glucose, positioning it as a vital biomarker for diabetes. Furthermore, the interaction of glucose with P@AlNNT displayed a lower energy gap of 0.545eV, suggesting that P@AlNNT exhibits higher reactivity compared to P@GaNT.

Furthermore, the quantum chemical descriptors such as chemical hardness ( $\eta$ ), softness ( $S$ ), chemical potential ( $\mu$ ), electronegativity ( $X$ ), and electrophilicity index ( $\omega$ ) which shade lighter on the kinetic stability and reactivity of complexes was further obtained from the HOMO- LUMO values [56]. Quantum chemical reactivity descriptors are essential tools to describe the reactivity and stability of a molecule [57,58]. Two very important parameters that determine the kinetic stability and reactivity of the systems under investigation are softness ( $S$ ) and hardness ( $\eta$ ) [53]. If the chemical hardness ( $\eta$ ) is small, the reactivity of a molecule is great, which is due to lower needed energy to promote an electron from the HOMO to LUMO orbitals [60]. In general, molecules with low hardness values are more reactive and may be more likely to participate in chemical reactions. [61]. The chemical hardness is decreased for studied surfaces after complexation with Glucose, fructose and xylose. However, xylose had the highest chemical hardness values of 2.204eV and 2.149eV for P@AlNNT and P@GaNT respectively. The highest softness value was obtained from the G\_P@AlNNT complex while the lowest is observed from X\_P@AlNNT system which is in close range with the values for pure P@AlNNT and P@GaNT. Again, an increase in chemical potential is observed for the interacted systems as against the pristine P@AlNNT and

P@GANNT surfaces and this depicts the electron flow direction. The reactivity order for the chemical potential is presented as  $-1.817 > -1.823 > -2.302 > -2.272 > -3.891 > -4.082$  for G\_P@AlNNT, G\_P@AlNNT, F\_P@AlNNT, F\_P@AlNNT, X\_P@AlNNT and X\_P@AlNNT respectively. From the chemical hardness order, the G\_P@AlNNT is greater than G\_P@AlNNT, showing more stability and low reactivity of this complex. Electrophilicity index shows the stabilization of a system when requires a further electronic charge from the environment [62,63].

To establish a solid foundation for biomedical applications and ensure the reliability of experiments, it is crucial to consider the influence of the solvent [64]. Consequently, we have investigated the impact of the interaction between sugars and the surfaces under study in a solvent phase. In this context, water has been chosen as the solvent medium, mirroring the human biological system and aligning with prior research endeavors [65]. The effect of the solvent, specifically water, on the kinetic stability and reactivity of the studied systems has been thoroughly examined. The results indicate that these systems exhibit greater stability than reactivity in water, as evidenced by the observed increase in the energy gap for all systems when measured in an aqueous environment. These findings are consistent with the research conducted by Singla and colleagues [66]. In contrast, Yin and associates reported negligible solvent effects on the electronic properties of adsorption behaviors involving H, O, OH, and H<sub>2</sub>O on the Fe (110) surface. However, as depicted in Table 2, our data shows a reduction in the HOMO and LUMO values of the studied systems when compared to the nanotubes before interaction. Furthermore, Fig. S1 reveal that the HOMO of P@AlNNT and P@GaNT nanotubes is frequently located on the doped phosphorus atoms and certain atoms of the interacting sugar molecules, while the LUMO is evenly distributed within the nanotubes employed in this study. Noteworthy changes are observed in the HOMO and LUMO during the interaction of fructose, glucose, and xylose with the nanotubes. In both P@AlNNT and P@GaNT complexes, the LUMO is situated on the phosphorus atoms. This suggests that the phosphorus atoms act as electron donors, while the surface serves as an electron acceptor, thereby elucidating the charge transfer dynamics between the tube, the doped phosphorus, and the respective sugar moieties. Fig. 3a and b depict the total electronic density of states (DOS) plots of the P@GaNT and P@AlNNT nanotubes, respectively, after the adsorption of the studied molecules. Based on this Figure, the adsorption of these biomarkers reduces the band gap of P@GaNT and P@AlNNT nanotube. Therefore, change of charge density takes place upon adsorption of fructose, glucose and xylose on the nanotube.

### 3.3. Vibrational frequencies

Vibrational spectroscopy leverages molecular vibrations to deduce

**Table 2**  
HOMO, LUMO, Energy gap and quantum descriptors of the studied system and complex optimized at the B3LYP-D3(BJ)/def2-SVP method.

| Systems        | HOMO   | LUMO    | $E_g$ eV | $\eta$ | $S$   | $X$   | $\mu$  | $\omega$ |
|----------------|--------|---------|----------|--------|-------|-------|--------|----------|
| P@AlNNT        | -6.422 | -1.768  | 4.654    | 2.327  | 0.214 | 4.095 | -4.095 | 3.600    |
| P@GaNT         | -6.259 | -1.959  | 4.300    | 2.150  | 0.232 | 4.109 | -4.109 | 3.926    |
| F_P@AlNNT      | -3.047 | -1.496  | 1.551    | 0.775  | 0.644 | 2.272 | -2.272 | 3.330    |
| F_P@GaNT       | -2.917 | -1.687  | 1.230    | 0.615  | 0.813 | 2.302 | -2.302 | 4.308    |
| G_P@AlNNT      | -2.367 | -1.278  | 0.545    | 0.273  | 1.835 | 1.823 | -1.823 | 6.097    |
| G_P@GaNT       | -2.167 | -1.468  | 0.699    | 0.349  | 2.861 | 1.817 | -1.817 | 4.723    |
| X_P@AlNNT      | -6.095 | -1.687  | 4.408    | 2.204  | 0.226 | 3.891 | -3.891 | 3.434    |
| X_P@GaNT       | -6.231 | -1.932  | 4.299    | 2.149  | 0.232 | 4.082 | -4.082 | 3.875    |
| Solvent(water) |        |         |          |        |       |       |        |          |
| P@AlNNT        | -6.258 | -1.442  | 4.815    | 2.407  | 0.207 | 3.850 | -3.850 | 3.078    |
| P@GaNT         | -6.149 | -1.768  | 4.380    | 2.190  | 0.456 | 3.958 | -3.958 | 3.576    |
| F_P@AlNNT      | -6.095 | -1.7143 | 4.381    | 2.190  | 0.456 | 3.904 | -3.904 | 3.478    |
| F_P@GaNT       | -6.040 | -1.414  | 4.626    | 2.313  | 0.432 | 3.727 | -3.727 | 3.002    |
| G_P@AlNNT      | -6.040 | -1.414  | 4.626    | 2.313  | 0.432 | 3.727 | -3.727 | 3.002    |
| G_P@GaNT       | -5.959 | -1.768  | 4.191    | 2.095  | 0.238 | 3.863 | -3.863 | 3.560    |
| X_P@AlNNT      | -6.013 | -1.414  | 4.599    | 2.299  | 0.434 | 3.713 | -3.713 | 2.997    |
| X_P@GaNT       | -6.231 | -1.904  | 4.327    | 2.163  | 0.462 | 4.967 | -4.067 | 3.822    |

molecular structure and local surroundings, encompassing aspects like solvation effects, ion pairing, intermolecular interaction strengths, and ion-molecule binding [67]. It plays pivotal roles in discerning intricate combination compounds. Analyzing how molecular vibrations respond to both intra- and intermolecular forces allow for the interpretation of a molecule's immediate environment [56,69]. Frequency shifts provide insights into the energies of molecular orbitals. The primary techniques employed for this purpose are infrared and Raman spectroscopy. Despite probing the same range of vibrational states, their intensity spectra exhibit notable distinctions due to differences in the excitation processes [70,71]. To assess the stability of the studied complexes, their vibrational frequencies were investigated in this study. Specifically, F\_P@AlNNT demonstrates 365 distinct vibrational modes, all of which exhibit positive frequencies, indicating the stability of this complex. Similarly, F\_P@GaNT exhibits 366 vibrational modes, and X\_P@AlNNT displays 354 observed vibrational modes. The following vibrations were observed in the complexes;

### 3.3.1. O—H vibrations

In F\_P@AlNNT, the O—H vibrations is observed within the range of  $3820.33\text{cm}^{-1}$ -  $3704.38\text{cm}^{-1}$ . The obtained values are higher than those reported in previous studies [72]. This increase may be a result of the repulsive effect within the complex. In, F\_P@GaNT, the observed O—H stretching vibration peak is within the range  $3824.83$ - $3640.50\text{cm}^{-1}$  which is above the expected range of O—H vibrations. In G\_P@AlNNT,

this stretching vibration is observed at frequency peaks  $3806.21$  and  $3739.09\text{cm}^{-1}$ . Also, in G\_P@GaNT, the observed vibration occurs at  $3824.19$  and  $3683.60\text{cm}^{-1}$ . In X\_P@AlNNT, the O—H stretching vibration was observed at frequency peak range  $3815.91$ - $3773.50\text{cm}^{-1}$  while in X\_P@GaNT, the O—H vibration occurs at frequency range  $3723.24$  and  $3683.60\text{cm}^{-1}$

### 3.3.2. N—H vibrations

The N—H stretching vibration is expected in the range  $3500$ - $3200\text{cm}^{-1}$ . In F\_P@AlNNT, the N—H vibration is observed within the frequencies  $3569.38$ - $3564.39\text{cm}^{-1}$ , which is higher than the expected peak. In F\_P@GaNT, The N—H vibration is observed within the range  $3571.34$  and  $3067.12\text{cm}^{-1}$ , higher than the expected range of N—H vibrations. In G\_P@AlNNT, the N—H vibration is observed at peaks  $3571.09$ , and  $3535.41\text{cm}^{-1}$ , while in G\_P@GaNT, it is observed at  $3581.53$  and  $3533.79\text{cm}^{-1}$ . The N—H vibrations observed in X\_P@AlNNT and X\_P@GaNT occurred at frequencies higher than the expected range as represented in Table 3.

### 3.3.3. Al-H vibrations

In F\_P@AlNNT, The Al-H stretching vibration is observed within the range of  $1901.79$ - $1885.57\text{cm}^{-1}$ . On the other hand, the G\_P@AlNNT Al-H vibration occurred at  $1929.30\text{cm}^{-1}$ . Also, in X\_P@AlNNT, this vibration is within the range of  $1909.57$ - $1894.35\text{cm}^{-1}$ .

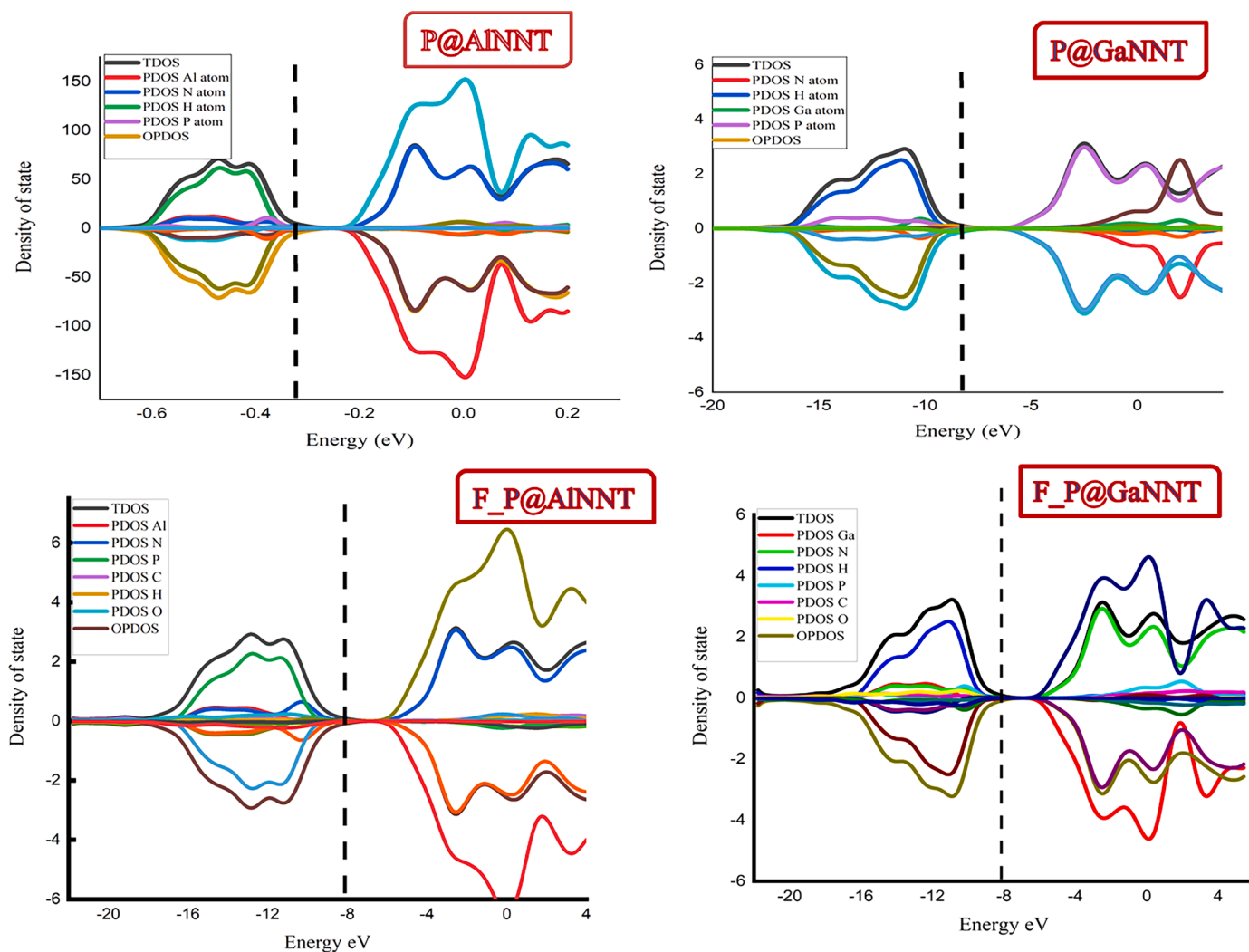


Fig. 3. (a). Density of state (DOS) plot of surface and complexes. (b): Density of state (DOS) plot of surface and complexes.

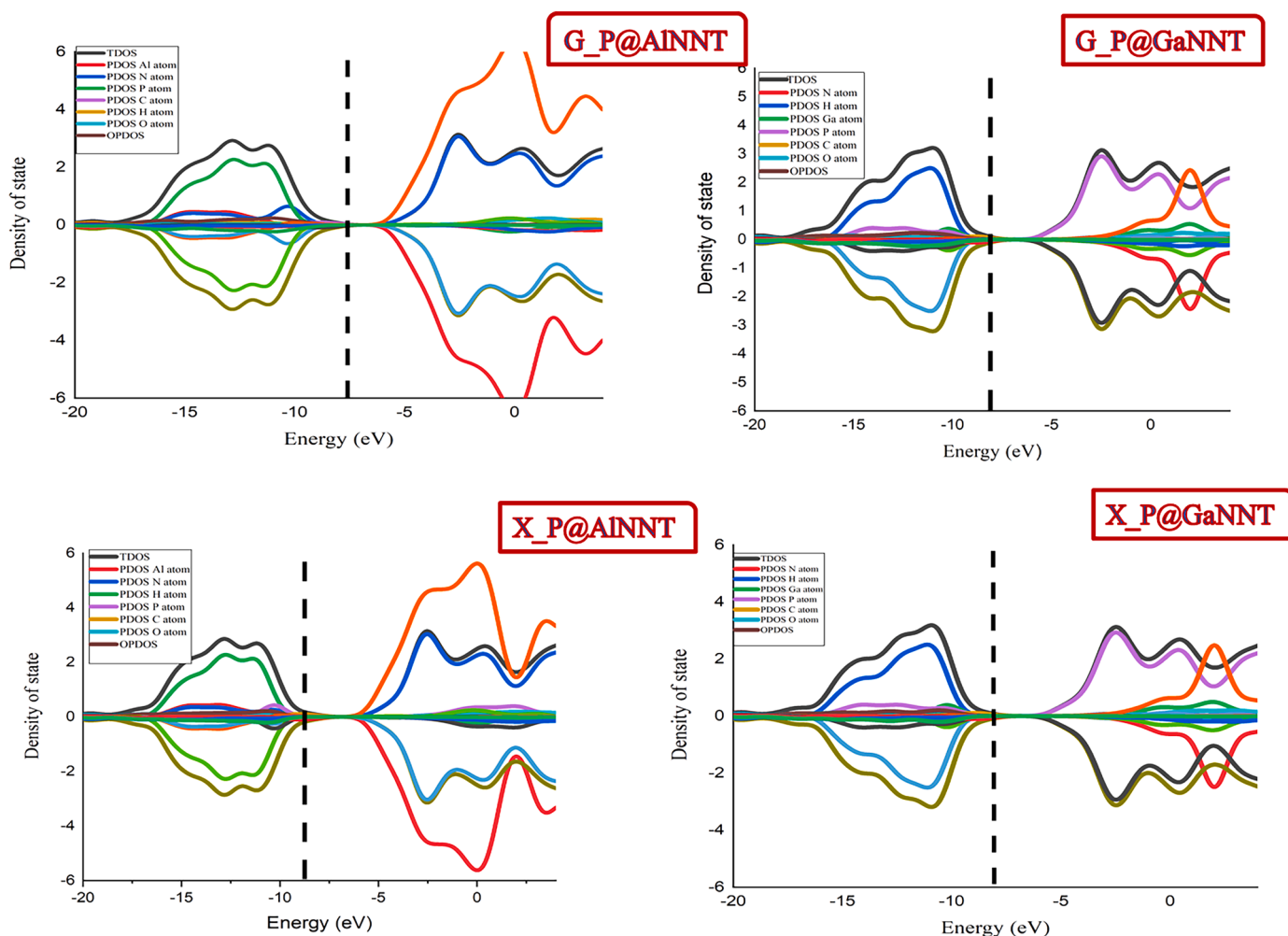


Fig. 3. (continued).

### 3.3.4. Ga-H vibrations

In F\_P@GaNT, the Ga-H stretching vibration is observed at frequency peak of  $1948.88\text{ cm}^{-1}$ . Also, in G\_P@GaNT, the Ga-H vibration occurs at a frequency of  $1968.29\text{ cm}^{-1}$  which is higher than the frequency peak observed in F\_P@GaNT system. The Ga-H stretching vibration occurs at frequencies  $1962.64$  and  $1953\text{ cm}^{-1}$  in X\_P@GaNT, which are higher as compared to the observed peak in F\_P@GaNT and lower when compared to G\_P@GaNT.

### 3.3.5. CH vibrations

The expected range of C-H stretching vibration as reported by Garrido and colleagues is within the range of  $3200\text{--}2800\text{ cm}^{-1}$  [73]. In F\_P@AlNNT, the CH stretching vibration is observed at frequency range of  $3144.98\text{--}3076.21\text{ cm}^{-1}$ , while in F\_P@GaNT, it occurs at  $3049.10\text{ cm}^{-1}$  all within the expected range of CH stretching vibration as reported in previous studies [73]. The observed C-H stretching vibration in X\_P@AlNNT was at the peak  $3151.95\text{ cm}^{-1}$  while in X\_P@GaNT the C-H stretching vibration is observed within the range of  $3110.03\text{--}2992.55\text{ cm}^{-1}$ . The C-H vibration obtained in all complexes were observed to be within the expected range.

## 3.4. Second order perturbation energy analysis

The concept of Natural Bond Orbital (NBO) analysis was developed based on the principles of localized electron-pair bonding units and the first-order reduced density matrix of the wavefunction [74]. In the NBO methodology, a given wavefunction is transformed into a localized

representation where NBOs are treated as local block eigenfunctions of the density matrix. This analytical approach is applicable to both closed-shell and open-shell systems, employing atom-centered basis functions [53]. Energetic assessments of NBO interactions hinge on the one-electron effective energy operator, typically derived from the electronic structure system, such as the Fock or Kohn-Sham matrix [60]. The second-order perturbation theory stands as one of the widely adopted methodologies for estimating energy effects [75]. Within the framework of Density Functional Theory (DFT), interactions between NBOs are explored to energetically evaluate the wavefunction, utilizing Kohn-Sham matrix elements for elucidation [58,75]. The notion of bound orbitals is employed to gain insights into the distribution of electrons in atomic and molecular orbitals [76]. These orbitals can be derived using atomic charges and molecular bonds [75]. In this process, an electron density matrix serves a dual purpose, characterizing the geometries of atomic orbitals within the molecular environment and identifying molecular bonds by assessing electron density between atoms. Non-stationary effects, such as the anomeric effect, rotation barriers, and hydrogen bonding, are scrutinized using binding orbital analysis [77]. NBO analysis dissects molecular energy into two distinct components: overall energy, which accounts for non-stationary elements, and Lewis molecular energy, where super-conjugation is absent, and electrons predominantly occupy single bonds and pairs [58,77]. Non-occupied NBOs play a crucial role in characterizing non-covalent interactions within the molecule. Furthermore, the assessment of donor-acceptor interactions in the NBO framework is carried out through second-order perturbation methods [78].

**Table 3**

FT-IR of the studied complexes optimized at the B3LYP-D3(BJ)/def2-SVP method.

| Systems   | Modes | Frequency $\text{cm}^{-1}$ | Assignment                              |
|-----------|-------|----------------------------|---|
| F_P@AlNNT | 1     | 3820.33                    | O-H stretching                          |
|           | 2     | 3704.38                    | O—H wagging                             |
|           | 3     | 3569.38                    | N-H stretching                          |
|           | 4     | 3564.39                    | N—H stretching                          |
|           | 5     | 3175.39                    | CH <sub>2</sub> asymmetrical stretching |
|           | 6     | 3144.98, 3076.21           | CH stretching                           |
|           | 7     | 1901.79, 1885.57           | Al-H stretching                         |
| F_P@GaNNT | 8     | 3824.83, 3640.50           | O-H stretching                          |
|           | 9     | 3571.34, 3067.12           | N—H stretching                          |
|           | 10    | 3049.10                    | C-H stretching                          |
|           | 11    | 3009.76                    | CH <sub>2</sub> stretching              |
|           | 12    | 1948.88                    | Ga—H stretching                         |
| G_P@AlNNT | 13    | 3806.21, 3739.09           | O-H stretching                          |
|           | 14    | 3571.09, 3535.41           | N—H stretching                          |
|           | 15    | 3153.29, 2991.93           | C-H stretching                          |
|           | 16    | 3084.00                    | CH <sub>2</sub> stretching              |
|           | 17    | 1929.30                    | Al—H stretching                         |
|           | 18    | 3824.19, 3683.60           | O-H stretching                          |
| G_P@GaNNT | 19    | 3581.53, 3533.79           | N—H stretching                          |
|           | 20    | 3132.11                    | CH <sub>2</sub> asymmetric stretching   |
|           | 21    | 3037.26                    | CH stretching                           |
|           | 22    | 1968.29                    | Ga-H stretching                         |
| X_P@AlNNT | 23    | 3815.91, 3773.50           | O-H stretching                          |
|           | 24    | 3579.45, 3562.29           | N—H stretching                          |
|           | 25    | 3158.41, 3087.60           | CH <sub>2</sub> stretching              |
|           | 26    | 3151.95                    | CH stretching                           |
|           | 27    | 1909.57, 1894.35           | Al-H stretching                         |
| X_P@GaNNT | 28    | 3723.24, 3683.60           | O-H stretching                          |
|           | 29    | 3578.60, 3572.12           | N—H stretching                          |
|           | 30    | 3110.03, 2992.55           | C-H stretching                          |
|           | 31    | 1962.64, 1953              | Ga—H stretching                         |

The NBO analysis simplifies the quantum-mechanical wave function into a formalism akin to Lewis dots. Non-Lewis-type NBOs are denoted as "empty" or "acceptor" orbitals ( $\pi^*$ ), while Lewis-type NBOs are described as "full" or "donor" orbitals ( $\pi$ ). The findings of this study suggest that the stabilization of F\_P@AlNNT is a consequence of interactions between bonding  $\pi$  (Al1-N2) and antibonding lone pair LP\* (Al9), yielding a significant stabilization energy of 28.16kcal/mol. Additionally, this system experiences stabilization from the bonding ( $\pi$ ) interaction of Al6-N8 with the antibonding lone pair (LP\*) (Al9), contributing a stabilization energy of 19.10kcal/mol. Other notable interactions within this system encompass  $\pi$ - $\pi^*$  (Al3-N4) - (Al14-N16) and  $\sigma^*$ - $\sigma^*$  (O102-C103) - (P100-O102). These interactions are summarized in Table 4. In F\_P@GaNNT, the system derives substantial stabilization from the  $\pi$  (N6-Ga87) - LP\*(Ga96) interaction, yielding an energy value of 24.04kcal/mol. Furthermore, a stabilization energy of 21.95kcal/mol is attributed to the interaction between  $\pi^*$ (N3-Ga68) and  $\pi^*$ (N4-Ga89). Other interaction found in this system is  $\pi$ - $\pi^*$  (N7-Ga88) - (N4-Ga89). Furthermore, in G\_P@AlNNT, the highest stabilization energy of interaction is obtained from the  $\pi$  (Al1-N2) - LP\*(1) (Al9). While other interactions involved in the overall stability of this complex include  $\pi$ - $\pi^*$  (Al3-N4) - (Al5 - N7) and (Al3 - N4) - (Al14 - N16). The G\_P@GaNNT complex is greatly stabilized by the  $\pi$  (N4-Ga89) - LP\*(1) (Ga98) with an energy of 23.69kcal/mol, while  $\pi$ - $\pi^*$  (N3-Ga68) - (N4-Ga89) has energy value of 22.80kcal/mol. Other  $\pi$ - $\pi^*$  interaction had stabilization energy values of 16.59Kcal/mol, 20.49Kcal/mol, 15.53Kcal/mol and 14.60Kcal/mol respectively. In this interaction, the sigma bonds create the framework that holds all the atoms together. Both X\_P@AlNNT and X\_P@GaNNT are stabilized by  $\pi$ -LP\* interactions with the highest stabilization energy obtained for both interactions.

### 3.5. Quantum theory of atom in molecule (QTAIM) analysis

Bader and colleagues [79] proposed the QTAIM approach which suggest that the critical point of the electron density, which can be a

**Table 4**

Second order perturbation energy of the studied systems optimized at the B3LYP-D3(BJ)/def2-SVP method.

| Systems   | Donor   | Acceptor                                      | E <sup>2</sup> kcal/mol | E(j)-E(i) | F(i,j) |
|-----------|---|---|-------------------------|-----------|--------|
| F_P@AlNNT | $\pi$ Al <sub>1</sub> -N <sub>2</sub>         | LP*Al <sub>9</sub>                            | 28.16                   | 0.24      | 0.075  |
|           | $\pi$ Al <sub>3</sub> -N <sub>4</sub>         | $\pi^*$ Al <sub>14</sub> -N <sub>16</sub>     | 19.10                   | 0.30      | 0.068  |
|           | $\pi$ Al <sub>5</sub> -N <sub>7</sub>         | $\pi^*$ Al <sub>6</sub> -N <sub>8</sub>       | 18.88                   | 0.30      | 0.067  |
|           | $\pi$ Al <sub>6</sub> -N <sub>8</sub>         | LP*Al <sub>9</sub>                            | 19.10                   | 0.24      | 0.061  |
|           | $\sigma^*$ O <sub>102</sub> -C <sub>103</sub> | $\sigma^*$ P <sub>100</sub> -O <sub>102</sub> | 10.04                   | 0.14      | 0.054  |
| F_P@GaNNT | $\pi^*$ N <sub>3</sub> -Ga <sub>68</sub>      | $\pi^*$ N <sub>4</sub> -Ga <sub>89</sub>      | 21.95                   | 0.27      | 0.068  |
|           | $\pi$ N <sub>3</sub> -Ga <sub>68</sub>        | $\pi^*$ N <sub>2</sub> -Ga <sub>70</sub>      | 15.17                   | 0.27      | 0.061  |
|           | $\pi$ N <sub>4</sub> -Ga <sub>89</sub>        | LP* Ga <sub>98</sub>                          | 23.44                   | 0.23      | 0.067  |
|           | $\pi^*$ N <sub>6</sub> -Ga <sub>87</sub>      | LP*Ga <sub>96</sub>                           | 24.04                   | 0.23      | 0.068  |
|           | $\pi$ N <sub>7</sub> -Ga <sub>88</sub>        | $\pi^*$ N <sub>4</sub> Ga <sub>89</sub>       | 16.76                   | 0.26      | 0.059  |
| G_P@AlNNT | $\pi$ Al <sub>1</sub> -N <sub>2</sub>         | LP*Al <sub>9</sub>                            | 28.11                   | 0.24      | 0.075  |
|           | $\pi$ Al <sub>3</sub> -N <sub>4</sub>         | $\pi^*$ Al <sub>5</sub> -N <sub>7</sub>       | 15.25                   | 0.30      | 0.061  |
|           | $\pi$ Al <sub>3</sub> -N <sub>4</sub>         | $\pi^*$ Al <sub>14</sub> -N <sub>16</sub>     | 19.14                   | 0.30      | 0.068  |
| G_P@GaNNT | $\pi$ N <sub>1</sub> -Ga <sub>90</sub>        | $\pi^*$ N <sub>3</sub> -Ga <sub>68</sub>      | 14.60                   | 0.29      | 0.059  |
|           | $\pi$ N <sub>2</sub> -Ga <sub>70</sub>        | $\pi^*$ N <sub>38</sub> -Ga <sub>72</sub>     | 15.53                   | 0.27      | 0.058  |
|           | $\pi$ N <sub>2</sub> -Ga <sub>70</sub>        | $\pi^*$ N <sub>7</sub> -Ga <sub>88</sub>      | 20.49                   | 0.25      | 0.065  |
|           | $\pi$ N <sub>3</sub> -Ga <sub>68</sub>        | $\pi^*$ N <sub>2</sub> -Ga <sub>70</sub>      | 16.59                   | 0.25      | 0.062  |
|           | $\pi$ N <sub>3</sub> -Ga <sub>68</sub>        | $\pi^*$ N <sub>4</sub> -Ga <sub>89</sub>      | 22.80                   | 0.27      | 0.070  |
| X_P@AlNNT | $\pi$ N <sub>4</sub> -Ga <sub>89</sub>        | LP*Ga <sub>98</sub>                           | 23.69                   | 0.23      | 0.068  |
|           | $\pi$ Al <sub>1</sub> -N <sub>2</sub>         | LP*Al <sub>9</sub>                            | 28.12                   | 0.24      | 0.075  |
|           | $\pi$ Al <sub>3</sub> -N <sub>4</sub>         | $\pi^*$ Al <sub>5</sub> -N <sub>7</sub>       | 15.19                   | 0.30      | 0.060  |
|           | $\pi$ Al <sub>3</sub> -N <sub>4</sub>         | $\pi^*$ Al <sub>14</sub> -N <sub>16</sub>     | 19.09                   | 0.30      | 0.068  |
|           | $\pi$ Al <sub>6</sub> -N <sub>8</sub>         | LP*Al <sub>9</sub>                            | 19.10                   | 0.24      | 0.061  |
| X_P@GaNNT | $\pi$ Al <sub>11</sub> -N <sub>13</sub>       | $\pi^*$ N <sub>23</sub> -Al <sub>24</sub>     | 18.69                   | 0.30      | 0.067  |
|           | $\pi$ N <sub>1</sub> -Ga <sub>90</sub>        | $\pi^*$ N <sub>36</sub> -Ga <sub>68</sub>     | 15.95                   | 0.29      | 0.062  |
|           | $\pi$ N <sub>2</sub> -Ga <sub>70</sub>        | $\pi^*$ N <sub>7</sub> -Ga <sub>88</sub>      | 18.41                   | 0.26      | 0.062  |
|           | $\pi$ N <sub>3</sub> -Ga <sub>68</sub>        | $\pi^*$ N <sub>2</sub> -Ga <sub>70</sub>      | 18.76                   | 0.24      | 0.061  |
|           | $\pi$ N <sub>6</sub> -Ga <sub>87</sub>        | LP*Ga <sub>96</sub>                           | 23.69                   | 0.23      | 0.068  |
|           | $\pi$ N <sub>10</sub> -Ga <sub>95</sub>       | $\pi^*$ N <sub>6</sub> -Ga <sub>87</sub>      | 17.37                   | 0.28      | 0.063  |

minimum point, a maximum point, or a saddle point, can fall into one of the following four categories, according to this theory: atomic critical point (ACP), which denotes the geometrical position of an atom or nucleus (other than hydrogen) and geometrically represents a local maximum point of electron density in all three directions of space [80] bond critical point (BCP), which denotes a critical point related to a bond or physical or chemical interaction (in reality, this point represents a saddle point with two directions of maximum electron density and one direction of minimum electron density) [77] and chemical critical point (CCP), which denote (geometrically, this point is a local minimum point in all three directions of space) [64].

To gain a deeper understanding of the intermolecular interactions between the studied biomarkers and adsorbent nanostructures, we conducted QTAIM analysis. The molecular graphs of the optimized sugar complexes are presented in Fig. 4. Various topological parameters were employed to characterize these interactions, including electron densities ( $\rho(r)$ ) and their laplacian ( $\nabla^2\rho(r)$ ), local potential electron energy density ( $V(r)$ ), kinetic electron density ( $G(r)$ ), and total electron energy densities ( $H(r)$ ) at bond critical points (BCP). These BCPs are pivotal in elucidating electrostatic or covalent bonds formed through electron transfer or redistribution. Positive values of  $H(r)$  at the BCP denote closed-shell interactions, while negative values indicate shared interactions. The ratio of  $-G_b/V_b$  greater than one signifies non-covalent and electrostatically weak interactions, whereas a value less than one confirms a covalent nature in the interaction. Strong covalent interactions are characterized by both negative  $\nabla^2\rho(r)$  and  $H(r)$  values, weak electrostatic interactions exhibit positive  $\nabla^2\rho(r)$  and  $H(r)$  values, and a positive  $\nabla^2\rho(r)$  value coupled with a negative  $H(r)$  value suggests the partial presence of both covalent and electrostatic interactions, defining the covalent nature of these interactions. Furthermore, the electron density, represented by an elliptical bond, reflects its preferential accumulation on the bonding plate. Higher values of  $\epsilon$  indicate structural instability, while lower values imply stability.

In F\_P@AlNNT,  $-G(r)/V(r)$  values obtained for the interactions are greater than one which suggest the existence of non-covalent interaction between the atoms; N<sub>66</sub>-H<sub>120</sub>, O<sub>119</sub>-H<sub>110</sub>, O<sub>115</sub>-H<sub>114</sub> and H<sub>117</sub>-O<sub>117</sub>.

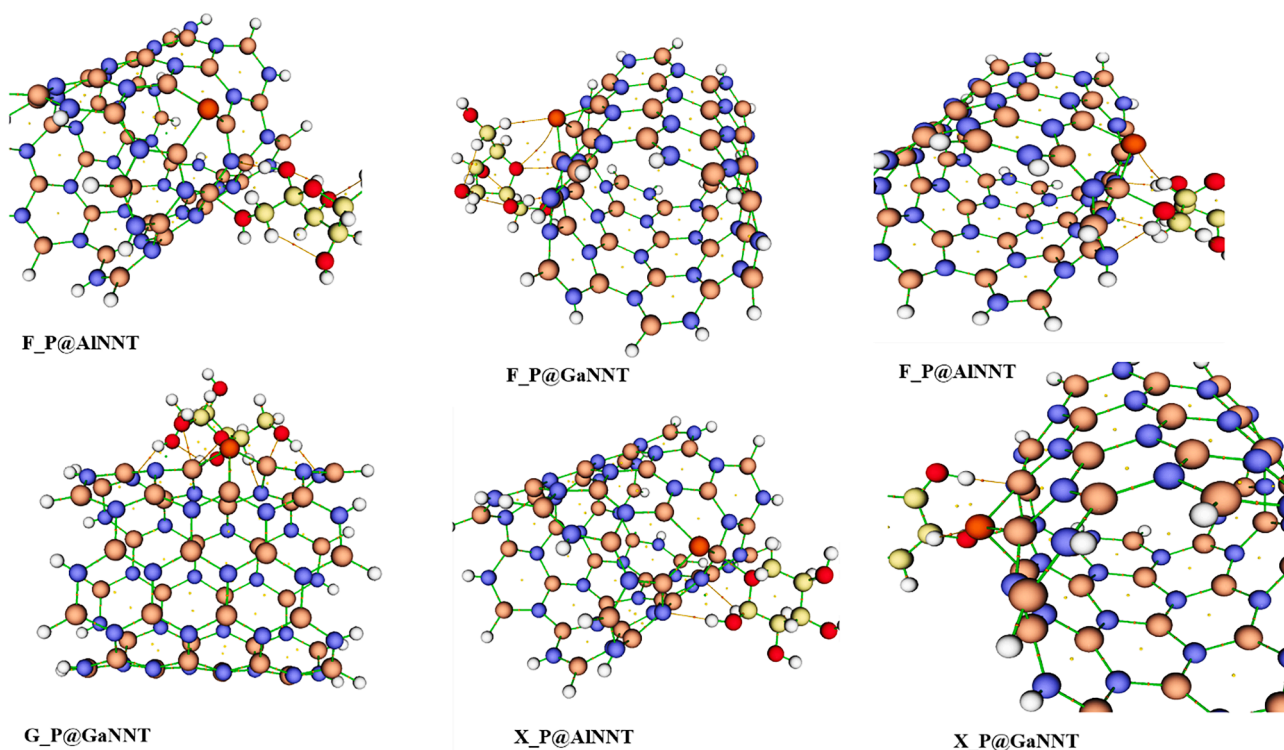


Fig. 4. Quantum theory of atom in molecules graph of the studied complexes.

Positive  $H(r)$  values obtained for  $O_{119}-H_{110}$ , and  $O_{115}-H_{114}$  interactions suggests the presence of covalent interaction within the complex, however, negative  $H(r)$  values of  $-0.221$  and  $-0.496$  obtained from  $N_{66}-H_{120}$  and  $H_{117}-O_{117}$  further strengthens the existence of covalent bond within this complex. Furthermore, the obtained result shows the existence of both electrostatic and covalent interaction within this complex as revealed by the positive  $V^2p(r)$  value with a negative  $H(r)$  value for  $N_{66}-H_{120}$ , and  $H_{117}-O_{117}$ . Furthermore, in  $F_P@GaNT$ , the  $G(r)/V(r)$  values were greater than one for  $O_{27}-H_{10}$  (1.095),  $O_{11}-H_{17}$  (1.400), and  $P_{100}-H_{110}$  (1.265) indicating the existence of electrostatically weak interactions between those atoms, however the interaction between  $P_{100}-O_{102}$  and  $O_{115}-H_{113}$  showed values less than one (0.612 and 0.613) representing a covalent interaction within this molecule. Low  $\epsilon$  values obtained for all the interactions in this  $F_P@GaNT$  system suggests that the system is stable.

In  $G_P@AlNNT$ , the  $H(r)$  values suggests the presence of both closed shell and covalent interactions between atoms in the complex since both positive and negative values were obtained for the interactions. In  $H_{120}-N_{36}$ , a covalent interaction was observed with  $H(r)$  value of  $-0.704$  while a weak electrostatic interaction is observed between  $O_{115}-H_{114}$  with  $H(r)$  value of 0.250. the existence of both covalent and non-covalent interactions in this system is strengthened by the presence of positive  $V^2p(r)$  value of 0.127 and negative  $H(r)$  value of  $-0.704$  for  $H_{120}-N_{36}$  interactions. Furthermore,  $G_P@GaNT$ , the  $-G(r)/V(r)$  values show the covalent nature of interaction found within the atoms;  $N_{31}-H_{124}$  (0.907) and  $Ga_{63}-O_{117}$  (0.432). This is further strengthened by the negative  $H(r)$  values;  $-0.291$  and  $-0.266$  obtained for each interaction respectively. As shown in Table 4, the intramolecular interaction within  $X_P@GaNT$  reveals the existence of both covalent and weak electrostatic interaction within the system on the basis of  $V^2P(r)$  and  $H(r)$  values. Also, in  $X_P@AlNNT$ , the  $-G(r)/V(r)$  value of 1.214 suggest the presence of electrostatic interaction between  $N_{36}-H_{100}$  atoms while the  $N_{39}-H_{114}$  shows the existence of non-covalent interaction. The  $V^2P(r)$  and  $H(r)$  values shows the existence of weakly electrostatic interaction within the  $N_{39}-H_{114}$  atoms. The ellipticity value  $\epsilon$  for all system showed values  $>1$  which shows stability of the

studied systems. Considering the LOL values of the interactions, a value of  $LOL > 0.5$ , indicates the localization of electron density, while interactions with  $LOL < 0.5$ , indicate the delocalization of electron density. In  $F_P@AlNNT$ , and  $F_P@GaNT$ , all LOL values were less than 0.5 which indicates that there is a localization of electron density. However, in  $G_P@AlNNT$ , the  $H_{120}-N_{36}$  and  $O_{115}-H_{114}$  interaction shows localization of electron density while  $H_{118}-O_{119}$  and  $O_{117}-H_{17}$  shows the delocalization of electron density with values greater than 0.5. In  $G_P@GaNT$  and  $X_P@AlNNT$ , the localization of electron density is observed in the interactions within the systems.

The Electron Localization Function (ELF) is a valuable metric for precisely characterizing molecular interactions from a chemical perspective while specifically delineating regions of electron delocalization [33]. ELF values are indicative of various electron density and interaction types, with larger ELF values associated with high electron density and covalent interactions, and smaller ELF values corresponding to low electron density and non-covalent interactions. This approach finds its roots in the Pauli principle, a fundamental concept used to elucidate numerous chemical phenomena, including aspects of the ELF [37]. Pauli's principle provides a clear explanation of the exchange repulsive effects and chemical bonding that occur between interacting molecules, addressing questions originally posed by Lewis [38]. ELF values falling within the range of 0.5 to 1 signify zones where bonding and nonbonding localized electrons are prevalent, indicating a tendency toward electron density homogeneity. Conversely, ELF values below 0.5 suggest the presence of delocalized electrons and hint at metallic characteristics. In our study, we utilized topological analysis of the Electron Localization Function to examine the nature of chemical bonding, and the results are presented in Table 5.

### 3.6. Noncovalent interaction (NCI) analysis

The conventional QTAIM criterion for analyzing electron density solely at critical points (CPs) has been a subject of controversy due to its exclusion of certain weak non-covalent interactions, notably  $\pi$ -stacking interactions [35]. To address this limitation, the Non-Covalent

Table 5

QTAIM table showing BCPs, ELF, LOL and other parameters.

| Complex   | Bond                               | CP                                | P(r)  | V <sup>2</sup> P(r) | G(r)  | K(r)   | V(r)   | H (r)  | -G(r)/V(r) | LOL    | ELF   | ε     |
|-----------|------------------------------------|-----------------------------------|-------|---------------------|-------|--------|--------|--------|------------|--------|-------|-------|
| F_P@AlNNT | N <sub>66</sub> -H <sub>120</sub>  | 253                               | 0.799 | 0.602               | 0.427 | 0.221  | -0.648 | -0.221 | 1.932      | 0.376  | 0.792 | 0.008 |
|           | O <sub>119</sub> -H <sub>110</sub> | 267                               | 0.285 | 0.124               | 0.288 | -0.236 | -0.264 | 0.236  | 1.090      | 0.210  | 0.661 | 0.182 |
|           | O <sub>115</sub> -H <sub>114</sub> | 198                               | 0.987 | 0.446               | 0.864 | -0.250 | -0.614 | 0.250  | 1.407      | 0.131  | 0.222 | 0.200 |
|           | H <sub>117</sub> -O <sub>117</sub> | 270                               | 0.850 | 0.363               | 0.702 | -0.206 | -0.496 | -0.496 | 1.415      | 0.126  | 0.204 | 0.299 |
| F_P@GaNTT | O <sub>27</sub> -H <sub>10</sub>   | 140                               | 0.281 | 0.125               | 0.288 | -0.248 | -0.263 | 0.248  | 1.095      | 0.206  | 0.630 | 0.192 |
|           | O <sub>11</sub> -H <sub>17</sub>   | 139                               | 0.989 | 0.386               | 0.749 | -0.216 | -0.532 | 0.216  | 1.400      | 0.129  | 0.630 | 0.192 |
|           | P <sub>100</sub> -H <sub>110</sub> | 179                               | 0.975 | 0.281               | 0.581 | -0.121 | -0.459 | 0.121  | 1.265      | 0.180  | 0.459 | 0.013 |
|           | P <sub>100</sub> -O <sub>102</sub> | 324                               | 0.117 | 0.559               | 0.508 | 0.320  | -0.829 | -0.320 | 0.612      | 0.466  | 0.866 | 0.065 |
| G_P@AlNNT | O <sub>115</sub> -H <sub>113</sub> | 309                               | 0.114 | 0.535               | 0.495 | 0.312  | -0.807 | -0.312 | 0.613      | 0.462  | 0.847 | 0.027 |
|           | H <sub>120</sub> -N <sub>36</sub>  | 233                               | 0.492 | 0.127               | 0.389 | 0.704  | -0.460 | -0.704 | 0.845      | 0.191  | 0.191 | 0.008 |
|           | H <sub>118</sub> -O <sub>119</sub> | 267                               | 0.285 | 0.124               | 0.288 | -0.236 | -0.264 | 0.236  | 1.090      | 0.661  | 0.661 | 0.182 |
|           | O <sub>115</sub> -H <sub>114</sub> | 198                               | 0.987 | 0.446               | 0.864 | -0.250 | -0.614 | 0.250  | 1.407      | 0.466  | 0.222 | 0.200 |
| G_P@GaNTT | O <sub>117</sub> -H <sub>17</sub>  | 278                               | 0.804 | 0.607               | 0.430 | 0.223  | -0.653 | -0.223 | 0.658      | 0.804  | 0.377 | 0.016 |
|           | N <sub>31</sub> -H <sub>124</sub>  | 255                               | 0.370 | 0.102               | 0.283 | 0.291  | -0.312 | -0.291 | 0.907      | 0.294  | 0.148 | 0.026 |
|           | Ga <sub>63</sub> -O <sub>117</sub> | 150                               | 0.236 | -0.253              | 0.203 | 0.266  | -0.470 | -0.266 | 0.432      | -0.253 | 0.619 | 0.064 |
|           | X_P@AlNNT                          | N <sub>39</sub> -H <sub>114</sub> | 181   | 0.135               | 0.484 | 0.108  | -0.115 | -0.127 | 0.127      | 0.850  | 0.399 | 0.169 |
| X_P@GaNTT | N <sub>36</sub> -H <sub>100</sub>  | 232                               | 0.161 | 0.669               | 0.142 | -0.248 | -0.117 | 0.248  | 1.214      | 0.172  | 0.414 | 0.262 |
|           | Ga <sub>63</sub> -H <sub>118</sub> | 49                                | 0.194 | -0.117              | 0.316 | 0.294  | -0.294 | -0.294 | 1.074      | 0.998  | 0.999 | 0.000 |
|           | P <sub>100</sub> -H <sub>111</sub> | 153                               | 0.753 | 0.216               | 0.424 | -0.166 | -0.307 | 0.116  | 1.381      | 0.163  | 0.368 | 0.000 |

Interaction (NCI) index offers a broader perspective beyond QTAIM, identifying weak interactions in regions where CPs defined by QTAIM are absent [38]. The NCI index proves itself as a versatile tool for detecting areas featuring non-covalent interactions, especially when the Reduced Density Gradient (RDG) approaches zero at low electron densities, a relationship visualized through plotting RDG against  $\rho(r)$  [37]. This approach relies on the sign of the second eigenvalue of the electron density Hessian matrix ( $\lambda_2$ ) to differentiate between attractive or bonding interactions and repulsive or non-bonding interactions [46]. By creating a 2D scatter plot of RDG against the product of  $\text{sign}(\lambda_2)$  and  $\rho(r)$  (i.e.,  $\text{sign}(\lambda_2) \rho(r)$ ), it effectively segregates attractive from repulsive non-covalent interactions. Additionally, the visualization of  $\text{sign}(\lambda_2) \rho(r)$  on a 3D RDG isosurface enhances our understanding of the type and

strength of non-covalent interactions through a color-coded representation. Here, blue denotes attractive contacts like hydrogen bonds and halogen bonds, green signifies very weak interactions such as van der Waals forces, and red represents steric repulsions [49]. The visual representation of the NCI isosurface was generated using the VMD program and is visible in Fig. 5.

In F\_P@AlNNT, the NCI plots reveal the presence of strong hydrogen bonds surrounding the doped phosphorus atom, likely attributable to its electronegativity. These hydrogen bonds are pivotal for anchoring the doped atom to the nanotube. However, a steric hindrance, represented by a ring, is observed at the phosphorus atom. This red ring signifies electron density depletion due to electrostatic repulsion, with its size indicating that there is minimal strain in the coordination sphere

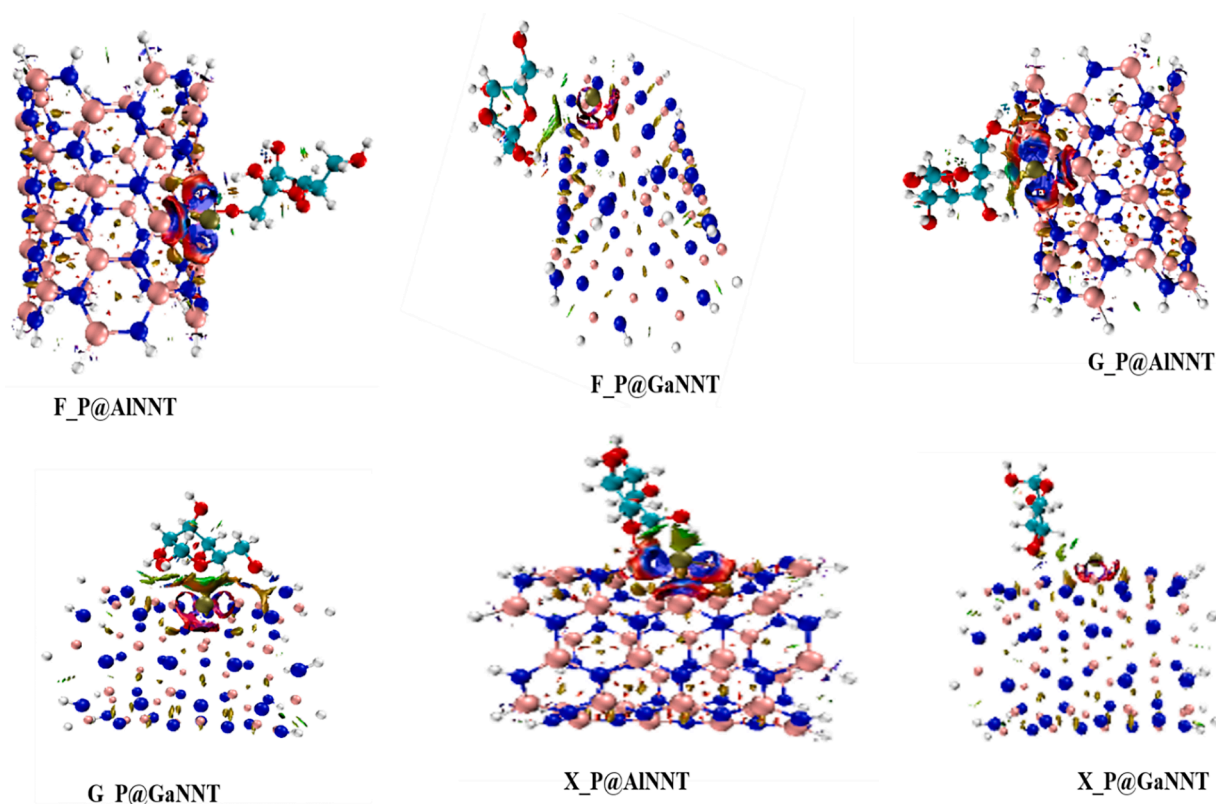


Fig. 5. Visualized NCI plots for studied complexes.

surrounding the central phosphorus and the aluminum atom [60]. Additionally, weak interactions such as  $\pi$ - $\pi$  stacking and other hydrogen bonds are observed within the nanotube, characterized by a subtle green coloration. Furthermore, dispersion interactions between the nanotubes are extensive and primarily confined to the regions between the two molecules. These dispersion forces play a substantial role in binding, contributing significantly to lowering the overall interaction energies of the complexes [63]. However, they do not notably impact the electron densities of the complexes. Furthermore, van der Waals interactions with minor steric hindrances are observed between the oxygen atom of the fructose molecule and the aluminum atom of the nanotube. This is depicted by the presence of both green and red patches surrounding the atom. The hydrogen bonds attached to the aluminum atom of the nanotube are surrounded by blue patches, signifying the presence of hydrogen bond interactions between these atoms. In the case of F\_GaNNT, there appears to be a lack of steric hindrances within the nanotube. The P@GaNNT complex is encircled by green patches, indicating weak van der Waals interactions. Interestingly, a strong non-bonded overlap is observed between the doped phosphorus atom and the nitrogen atom, represented by the red circular disk around these atoms. Additionally, traces of hydrogen bond interactions are present within both atoms, as evidenced by the blue patches adjacent to the red circular disk. The red ring in this context also signifies electron density depletion. Moreover, the nitrogen and oxygen atoms of fructose engage in strong van der Waals interactions, illustrated by the green patches between these atoms.

The same trend from F\_P@AlNNT is observed in G\_P@AlNNT however, a slight blue colored patch is observed within the hydrogen atom of the adsorbate glucose molecule and the phosphorus atom, indicating the existence of a weak hydrogen bond interaction between the glucose and the nanotube. These same interactions are displayed in the X\_P@AlNNT system as shown in Fig. 5. On interaction of Glucose to P@GaNNT (G\_P@GaNNT), the same interactions were observed, however, the later showed a strong van der waals interaction between the doped atom and the oxygen atom of the glucose molecule. Also, a strong hydrogen bond interaction is observed within the hydrogen atom and Gallium atom of the nanotube represented by a blue patch between those atoms. The same trend is observed on interaction of xylose to P@GaNNT (X\_P@GaNNT).

### 3.7. Adsorption studies

Adsorption constitutes a pivotal phenomenon across various scientific and engineering domains, including materials science, surface chemistry, and catalysis [81]. Its applications span a wide spectrum, encompassing gas separation, gas storage, and heterogeneous catalysis. In the realm of adsorbents and adsorbate characterization, methods such as adsorption isotherms, surface area measurements, and thermal analysis are employed [76]. At its core, adsorption refers to the process whereby molecules from a gas, liquid, or dissolved solid adhere to the surface of a solid or liquid substrate [82]. Two primary categories of adsorption commonly encountered are physisorption and chemisorption. In physisorption, biomarker molecules bind to the surface through weak van der Waals forces, which stem from attractive forces between molecules arising from transient dipoles. Conversely, chemisorption involves molecules undergoing a chemical reaction with the surface, resulting in the formation of robust chemical bonds [83]. Table 6 presents adsorption energy values, with F\_P@AlNNT and F\_P@GaNNT exhibiting negative values of  $-1.442\text{eV}$  and  $-1.469\text{eV}$ , respectively. These findings suggest that when fructose interacts with P@AlNNT and P@GaNNT, the fructose molecules become chemisorbed onto the tubes. Notably, the P@GaNNT interaction yields the most negative value ( $-1.469\text{eV}$ ), indicating stronger chemisorption. In contrast, glucose and xylose display physisorption characteristics when interacting with P@AlNNT and P@GaNNT. This is evident from the positive values obtained for the interactions of glucose with P@AlNNT ( $18.232\text{eV}$ ) and

**Table 6**

Adsorption energy and recovery time of the studied complexes optimized at the B3LYP-D3(BJ)/def2-SVP method.

| System    | E <sub>ad</sub> eV | Recovery time | E <sub>ad</sub> eV | Recovery time |
|-----------|--------------------|---------------|--------------------|---------------|
| F_P@AlNNT | -1.442             | 7.87E-12      | -1.458             | 2.25E-11      |
| F_P@GaNNT | -1.469             | 8.18E-12      | -1.487             | 7.28E-12      |
| G_P@AlNNT | 18.232             | 4.70E-24      | 18.234             | 4.70E-12      |
| G_P@GaNNT | 19.375             | 9.17E-25      | 17.088             | 9.17E-13      |
| X_P@AlNNT | 14.367             | 1.18E-21      | 14.386             | 8.66E-22      |
| X_P@GaNNT | 14.422             | 1.09E-21      | 14.430             | 1.33E-22      |

P@GaNNT ( $19.375\text{eV}$ ). The physisorption of glucose is attributed to the weak van der Waals interactions binding the glucose molecule to these nanostructures. Similarly, xylose is adsorbed onto the surfaces of P@AlNNT and P@GaNNT with adsorption energies of  $14.367\text{eV}$  and  $14.422\text{eV}$ , respectively. Adsorption was observed to increase in the solvent phase, the adsorption energy of F\_P@AlNNT in the solvent was  $-1.458\text{eV}$ , which is greater than the;  $-1.442\text{eV}$  observed in the gas phase. In the gas phase of F\_P@GaNNT, an adsorption energy of  $-1.469\text{eV}$  was observed, while an energy value of  $-1.487\text{eV}$  was obtained in the solvent phase. The energy value of physisorption of glucose in G\_P@AlNNT was  $18.232\text{eV}$  in the gas phase and  $18.234\text{eV}$  in the aqueous phase. The difference in adsorption energies observed in this complex for both phases is negligible. However, in G\_P@GaNNT, an adsorption energy of  $19.375\text{eV}$  is observed on the adsorption of glucose in the gas phase while a lower physisorption value of  $17.088\text{eV}$  is observed, indicating that glucose is less physisorbed in the gas phase than in the water phase, favoring chemisorption in the aqueous phase. In addition, X\_P@AlNNT, in aqueous phase the adsorption energy of  $17.088\text{eV}$  was obtained, while in gas phase adsorption energy of  $14.367\text{eV}$  was observed. Furthermore, in the gas phase of X\_P@AlNNT, a lower adsorption energy of  $14.422\text{eV}$  was observed, while  $14.430\text{eV}$  was observed in the aqueous phase. Because the solvent tends to mimic the human body system, the higher adsorption energies obtained in the solvent suggest a favorable application of these systems in the human body. The biomarkers fructose, glucose, and xylose may be detected by the phosphorus-doped AlNNT and GaNNT based on the displayed attributes of these interactions.

#### 3.7.1. Recovery time

Recovery time in the context of adsorption refers to the amount of time it takes for an adsorbent material to regenerate or regain its adsorption capacity after being employed to remove or absorb a certain substance [84]. The recovery time for adsorption is dependent on a number of variables, including the type and qualities of the adsorbent and adsorbate, the adsorption circumstances, and the nature of the regeneration process. The sensor device's recovery time is also a significant criterion for evaluation purposes [85]. The recovery time can be described using the traditional transition state theory with the Eq. (12).

$$\tau = V_0^{-1} e^{-E_{ad}/KT} \quad (12)$$

Where K designates the Boltzmann constant which approximately  $\sim 2.0 \times 10^{-3} \text{kcal/mol}$ . K,  $V_0$  is the attempt frequency and T is the temperature. Hence, an increase in adsorption energy results in an exponential lengthening of the recovery time as shown in Table 6. Longer recovery time of 7.8s and 8.1s was observed for F\_P@AlNNT and F\_P@GaNNT systems which strengthens the result obtained for adsorption of fructose, shorter recovery time was observed for glucose on P@AlNNT and xylose on P@AlNNT and P@GaNNT with values 4.70s, 1.1s and 1.09s respectively. An interesting difference in the recovery time of glucose from P@GaNNT is observed with a value of 9.17s which is higher than the recovery time of each biomarker in the studied systems.

**Table 7**  
Thermodynamics properties of the studied systems.

| Complex    | $\Delta H$ | Entropy | $\Delta G$ |
|------------|------------|---------|------------|
| F_P@AlNNT  | -0.735     | 507.346 | -0.494     |
| F_P@GaNNNT | -0.706     | 622.700 | -0.410     |
| G_P@AlNNT  | -0.737     | 503.029 | -0.498     |
| G_P@GaNNNT | -0.713     | 606.975 | -0.424     |
| X_P@AlNNT  | -0.701     | 499.504 | -0.464     |
| X_P@GaNNNT | -0.682     | 578.203 | -0.387     |

### 3.7.2. Thermodynamics properties

Thermodynamics is the study of the interplay of work and heat with physical changes of state within the bounds of thermodynamic laws [45]. Thermodynamics addresses the link between properties of a system such as temperature, specific heat, and so on that may be effectively measured in order to acquire a better understanding of the interacting system [46]. Correct and in-depth understanding of thermodynamic laws allows us to efficiently research the free energy (G), entropy (S), enthalpy (H), and other properties of reacting systems, opening up the possibility of detecting the feasibility of adsorption of a studied metal with a gas [47]. Equations 9–11 were used to derive thermodynamic characteristics using the DFT method at a constant temperature of 298.15k. If the change in enthalpy of formation for a particular reaction is negative, it is called spontaneous; if it is positive, it is non-spontaneous. The Gibbs free energy for spontaneous reactions should be negative, but nonspontaneous reactions should have positive free Gibbs energy  $G > 0$ . Table 7 displays the enthalpy ( $\Delta H$ ), entropy (S), and free Gibbs energy (G) for the interacting surfaces. There was little to no variance in the values obtained for change in enthalpy and entropy of the various interactions. This is analogous to the trend noticed in the interacting surfaces' energy gaps. All of the G and H readings are negative, whereas S is positive.

The enthalpy of a system (H) is the sum of its internal energy and the volume and pressure products. Enthalpy is a function for many metrics in biological and chemical systems that aid in distinguishing between the products and reactants of a system. When  $\Delta H > 0$ , the reaction is considered to be endothermic; when  $\Delta H < 0$  it is said to be exothermic. In this study, the enthalpy of reaction for various nanotubes was calculated using data obtained from optimized interacted complexes and the results showed negative values ie  $\Delta H > 0$  which signifies an endothermic favorable reaction. Also, Gibbs free energy (G) is divided into two types: spontaneous and non-spontaneous. A large negative value for G indicates a thermodynamically favorable reaction []. A thermodynamic system's reversible function of work is computed using the system's Gibbs free energy ( $\Delta G$ ), which is a thermodynamic potential. For the studied systems, the  $\Delta G$  values reveal a thermodynamically favorable and spontaneous reaction within the systems as shown in Table 7. The entropy values obtained for the systems are in the order 622.700>606.975>578.203>507.346>503.029> 499.504 for F\_P@GaNNNT, G\_P@GaNNNT, X\_P@GaNNNT, G\_P@AlNNT, F\_P@AlNNT and X\_P@AlNNT respectively.

## 4. Conclusions

This paper investigated the adsorption and detection properties of phosphorus doped Gallium nitride nanotubes (GaNNNT) and Aluminium nitride nanotubes (AlNNT) for the detection of sugar molecules such as fructose, glucose, and xylose using DFT method. Adsorption energy, density of states, charge transfer, NCI, and QTAIM were used to investigate sugar adsorption on surfaces. The model surfaces are conductive and suitable for sugar adsorption after the HOMO is stabilized and the energy gap is narrowed. The substitution of phosphorus atoms to the surfaces of P@GaNNNT and P@AlNNT improves their selectivity and detection abilities. The conductive properties of the tested surfaces were validated by

the DOS plot. The NBO analysis yielded the following order of decreasing stabilization energy: 28.16 > 28.12 > 28.11 > 24.04 > 23.69 > 19.10 kcal/mol and confirms the stability of modelled surfaces for the adsorption of the investigated sugar molecule. According to the QTAIM analysis, non-covalent and covalent interactions exist during the adsorption of the studied sugars on the doped GaNNNT and AlNNT surfaces, which is consistent with the NCI results. Furthermore, our calculation of recovery time suggests that surfaces could be useful adsorbent and detecting materials. In addition, the adsorption energy was in the order of  $-1.487 > -1.458 > 14.386 > 14.430 > 17.088 > 18.234$  eV. Doping with phosphorus atoms improves surface adsorption properties. As a result, F\_P@GaNNNT has a chemisorption value of  $-1.469$  eV. At the surfaces, fructose was chemisorbed, whereas glucose and xylose were physisorbed.

## Declarations

*Ethics approval and consent to participate*

Not applicable.

*Consent for publication*

Not applicable.

*Availability of data and material*

All data are contained within the manuscript.

## Funding

This work was not funded by any agency.

## CRediT authorship contribution statement

**Anna Imojara:** Conceptualization, Formal analysis, Investigation, Project administration, Software, Supervision, Writing – original draft, Writing – review & editing. **Joyce E. Ishegbe:** Conceptualization, Formal analysis, Investigation, Project administration, Software, Supervision, Writing – original draft, Writing – review & editing. **Hewa Abdullah:** Conceptualization, Formal analysis, Investigation, Project administration, Software, Supervision, Writing – original draft, Writing – review & editing. **Henry O. Edet:** Conceptualization, Formal analysis, Investigation, Project administration, Software, Supervision, Writing – original draft, Writing – review & editing. **Terkumbur E. Gber:** Conceptualization, Formal analysis, Investigation, Project administration, Software, Supervision, Writing – original draft, Writing – review & editing. **Maxwell-Borjor A. Eba:** Conceptualization, Formal analysis, Investigation, Project administration, Software, Supervision, Writing – original draft, Writing – review & editing. **Anthony M.S. Pembere:** Conceptualization, Formal analysis, Investigation, Project administration, Software, Supervision, Writing – original draft, Writing – review & editing. **Hitler Louis:** Conceptualization, Formal analysis, Investigation, Project administration, Software, Supervision, Writing – original draft, Writing – review & editing.

## Declaration of Competing Interest

The authors declare that they have no known competing financial interests or personal relationships that could have appeared to influence the work reported in this paper.

## Data availability

No data was used for the research described in the article.

## Acknowledgments

The authors would like to acknowledge the center for high performance computing (CHPC), South Africa for providing computational resources for this research project.

## References

- [1] W.J. Dahl, M.L. Stewart, Position of the academy of nutrition and dietetics: health implications of dietary fiber, *J. Acad. Nutr. Diet.* 115 (11) (2015) 1861–1870.
- [2] P.D. Marsh, In sickness and in health—What does the oral microbiome mean to us? An ecological perspective, *Adv. Dent. Res.* 29 (1) (2018) 60–65.
- [3] H. Çolak, Ç.T. Dülgergil, M. Dalli, M.M. Hamidi, Early childhood caries update: a review of causes, diagnoses, and treatments, *J. Nat. Sci. Biol. Med.* 4 (1) (2013) 29.
- [4] R.A. DeFronzo, E. Ferrannini, L. Groop, R.R. Henry, W.H. Herman, J.J. Holst, R. Weiss, Type 2 diabetes mellitus, *Nat. Rev. Dis. Primers* 1 (1) (2015) 1–22.
- [5] D.H. Ipsen, J. Lykkesfeldt, P. Tveden-Nyborg, Molecular mechanisms of hepatic lipid accumulation in non-alcoholic fatty liver disease, *Cell. Mol. Life Sci.* 75 (2018) 3313–3327.
- [6] M.L. Macheda, S. Rogers, J.D. Best, Molecular and cellular regulation of glucose transporter (GLUT) proteins in cancer, *J. Cell. Physiol.* 202 (3) (2005) 654–662.
- [7] S. Hameed, L. Xie, Y. Ying, Conventional and emerging detection techniques for pathogenic bacteria in food science: a review, *Trends Food Sci. Technol.* 81 (2018) 61–73.
- [8] P. Mehrotra, Biosensors and their applications—A review, *J. Oral Biol. Craniofacial Res.* 6 (2) (2016) 153–159.
- [9] A.B. Peinado, M.A. Rojo-Tirado, P.J. Benito, Sugar and physical exercise; the importance of sugar for athletes, *Nutr. Hosp.* 28 (Supl 4) (2013) 48–56.
- [10] F. Maod, F. Dukalang, N.L. Arwati, Identification of organic compounds as carbohydrates and chemicals contained in them, *J. Health Technol. Sci. JHTS* 3 (1) (2022) 19–27.
- [11] K. Niaz, F. Khan, M.A. Shah, Analysis of carbohydrates (monosaccharides, polysaccharides). *Recent Advances in Natural Products Analysis*, Elsevier, 2020, pp. 621–633.
- [12] X. Qi, R.F. Tester, Fructose, galactose and glucose—In health and disease, *Clin Nutr ESPEN* 33 (2019) 18–28.
- [13] H. Jain, S. Mulay, A review on different modes and methods for yielding a pentose sugar: xylitol, *Int. J. Food Sci. Nutr.* 65 (2) (2014) 135–143.
- [14] M. Rajinipriya, M. Nagalakshmaiah, M. Robert, S. Elkoun, Importance of agricultural and industrial waste in the field of nanocellulose and recent industrial developments of wood based nanocellulose: a review, *ACS Sustain. Chem. Eng.* 6 (3) (2018) 2807–2828.
- [15] X. Qi, R.F. Tester, Lactose, maltose, and sucrose in health and disease, *Mol. Nutr. Food Res.* 64 (8) (2020), 1901082.
- [16] A. Alsalmeh, T. Pooventhiran, N. Al-Zaqri, D.J. Rao, S.S. Rao, R. Thomas, Modelling the structural and reactivity landscapes of tucatinib with special reference to its wavefunction-dependent properties and screening for potential antiviral activity, *J. Mol. Model.* 26 (2020) 1–17.
- [17] J.S. Al-Otaibi, A.H. Almuqrin, Y.S. Mary, R. Thomas, Modeling the conformational preference, spectroscopic properties, UV light harvesting efficiency, biological receptor inhibitory ability and other physico-chemical properties of five imidazole derivatives using quantum mechanical and molecular mechanics tools, *J. Mol. Liq.* 310 (2020), 112871.
- [18] G.D. Dimitriadis, E. Maratou, A. Kountouri, M. Board, V. Lambadiari, Regulation of postabsorptive and postprandial glucose metabolism by insulin-dependent and insulin-independent mechanisms: an integrative approach, *Nutrients* 13 (1) (2021) 159.
- [19] A. Cherkas, S. Holota, T. Mdzinarashvili, R. Gabbianelli, N. Zarkovic, Glucose as a major antioxidant: when, what for and why it fails? *Antioxidants* 9 (2) (2020) 140.
- [20] D.Y. Kim, A. Kadam, S. Shinde, R.G. Saratale, J. Patra, G. Ghodake, Recent developments in nanotechnology transforming the agricultural sector: a transition replete with opportunities, *J. Sci. Food Agric.* 98 (3) (2018) 849–864.
- [21] O. Marom, F. Nakhoul, U. Tisch, A. Shiban, Z. Abassi, H. Haick, Gold nanoparticle sensors for detecting chronic kidney disease and disease progression, *Nanomedicine* 7 (5) (2012) 639–650.
- [22] X. Zhang, R. Fang, D. Chen, G. Zhang, Using Pd-doped  $\gamma$ -graphyne to detect dissolved gases in transformer oil: a density functional theory investigation, *Nanomaterials* 9 (10) (2019) 1490.
- [23] U. Tisch, I. Schlesinger, R. Ionescu, M. Nassar, N. Axelrod, D. Robertman, H. Haick, Detection of Alzheimer's and Parkinson's disease from exhaled breath using nanomaterial-based sensors, *Nanomedicine* 8 (1) (2013) 43–56.
- [24] Z. Mohammadi, S.M. Jafari, Detection of food spoilage and adulteration by novel nanomaterial-based sensors, *Adv. Colloid Interface Sci.* 286 (2020), 102297.
- [25] H. Roohi, N.A. Ardehijani, Adsorption behaviour of NO, NO<sub>2</sub>, CO and CS<sub>2</sub> molecules on the surface of carbon-doped gallium nitride nanosheet: a DFT study, *Surf. Sci.* 717 (2022), 121988.
- [26] J.A. Shlaka, A.H.A. Nasria, Density functional theory study on the adsorption of AsH<sub>3</sub> gas molecule with monolayer (AlN) 21 (including pristine, C, B doped and defective aluminium nitride sheet), in: *Proceedings of the IOP Conference Series: Materials Science and Engineering* 928, IOP Publishing, 2020, 072082. No.
- [27] M.T. Baei, Y. Kanani, V.J. Rezaei, A. Soltani, Adsorption phenomena of gas molecules upon Ga-doped BN nanotubes: a DFT study, *Appl. Surf. Sci.* 295 (2014) 18–25.
- [28] M.J. Frisch, G.W. Trucks, H.B. Schlegel, G.E. Scuseria, M.A. Robb, J.R. Cheeseman, G. Scalmani, V. Barone, G.A. Petersson, H. Nakatsuji, X. Li, M. Caricato, A.V. Marenich, J. Bloino, B.G. Janesko, R. Gomperts, B. Mennucci, H.P. Hratchian, J.V. Ortiz, A.F. Izmaylov, J.L. Sonnenberg, D. Williams-Young, F. Ding, F. Lipparini, F. Egidi, J. Goings, B. Peng, A. Petrone, T. Henderson, D. Ranasinghe, V.G. Zakrzewski, J. Gao, N. Rega, G. Zheng, W. Liang, M. Hada, M. Ehara, K. Toyota, R. Fukuda, J. Hasegawa, M. Ishida, T. Nakajima, Y. Honda, O. Kitao, H. Nakai, T. Vreven, K. Throssell, J.A. Montgomery, Jr., J.E. Peralta, F. Ogliaro, M.J. Bearpark, J.J. Heyd, E.N. Brothers, K.N. Kudin, V.N. Staroverov, T.A. Keith, R. Kobayashi, J. Normand, K. Raghavachari, A.P. Rendell, J.C. Burant, S.S. Iyengar, J. Tomasi, M. Cossi, J.M. Millam, M. Klene, C. Adamo, R. Cammi, J.W. Ochterski, R.L. Martin, K. Morokuma, O. Farkas, J.B. Foresman, and D.J. Fox, Gaussian, Inc., Wallingford CT, 2016.
- [29] R. Dennington, T.A. Keith, J.M. Millam, *HyperChem 8.07*, HyperChem Professional Program, Gainesville, Hypercube, 2001, 2016.
- [30] J. Jeevanandam, A. Barhoum, Y.S. Chan, A. Dufresne, M.K. Danquah, Review on nanoparticles and nanostructured materials: history, sources, toxicity and regulations, *Beilstein J. Nanotechnol.* 9 (1) (2018) 1050–1074.
- [31] T. Lu, Q. Chen, A simple method of identifying  $\pi$  orbitals for non-planar systems and a protocol of studying  $\pi$  electronic structure, *Theor. Chem. Acc.* 139 (2) (2020) 25.
- [32] I. Jomaa, N. Issaoui, T. Roisnel, H. Marouani, Insight into non-covalent interactions in a tetrachlorocadmamate salt with promising NLO properties: experimental and computational analysis, *J. Mol. Struct.* 1242 (2021), 130730.
- [33] A.S. Kazachenko, N. Issaoui, A. Sagaama, Y.N. Malyar, O. Al-Dossary, L. G. Bousiakou, Z. Xiang, Hydrogen bonds interactions in biuret-water clusters: FTIR, X-ray diffraction, AIM, DFT, RDG, ELF, NLO analysis, *J. King Saud Univ. Sci.* 34 (8) (2022), 102350.
- [34] Z. Schnepf, Biopolymers as a flexible resource for nanochemistry, *Angew. Chem. Int. Ed.* 52 (4) (2013) 1096–1108.
- [35] Y. Luo, Food colloids binary and ternary nanocomplexes: innovations and discoveries, *Colloids Surf. B* 196 (2020), 111309.
- [36] S. Contera, J. Bernardino de la Serna, T.D. Tetley, *Biotechnology, nanotechnology and medicine, Emerging Topics in Life Sciences* 4 (6) (2020) 551–554.
- [37] H. Louis, T.E. Gber, F.C. Asogwa, E.A. Eno, T.O. Unimuke, V.M. Bassey, B.I. Ita, Understanding the lithiation mechanisms of pyrenetetrone-based carbonyl compound as cathode material for lithium-ion battery: insight from first principle density functional theory, *Mater. Chem. Phys.* 278 (2022), 125518.
- [38] D.O. Odey, H. Louis, D.K. Ita, H.O. Edet, P.B. Ashishie, T.E. Gber, A.G. Efa, Intermolecular interactions of cytosine DNA nucleoside base with gallic acid and its methylgallate and ethylgallate derivatives, *ChemistrySelect* 8 (9) (2023), e202203832.
- [39] R.A. Timothy, H. Louis, E.A. Adindu, T.E. Gber, E.C. Agwamba, O.E. Offiong, A. M. Pembere, Elucidation of collagen amino acid interactions with metals (B, Ni) encapsulated graphene/PEDOT material: insight from DFT calculations and MD simulation, *J. Mol. Liq.* 390 (2023), 122950.
- [40] R.M. Pashley, J.N. Israelachvili, Molecular layering of water in thin films between mica surfaces and its relation to hydration forces, *J. Colloid Interface Sci.* 101 (2) (1984) 511–523.
- [41] X. Zhao, G. Zhu, L. Jiao, F. Yu, C. Xie, Formation and extractive desulfurization mechanisms of aromatic acid based deep eutectic solvents: an experimental and theoretical study, *Chem. Eur. J.* 24 (43) (2018) 11021–11032.
- [42] E.C. Agwamba, H. Louis, P.O. Olagoke, T.E. Gber, G.A. Okon, C.F. Fidelis, A. S. Adeyinka, Modeling of magnesium-decorated graphene quantum dot nanostructure for trapping AsH<sub>3</sub>, PH<sub>3</sub> and NH<sub>3</sub> gases, *RSC Adv.* 13 (20) (2023) 13624–13641.
- [43] V. Krasnenko, L.L. Rusevich, A. Platonenko, Y.A. Mastrikov, M. Sokolov, E. A. Kotomin, Water splitting on multifaceted SrTiO<sub>3</sub> nanocrystals: calculations of raman vibrational spectrum, *Materials* 15 (12) (2022) 4233. Basel.
- [44] D.O. Odey, H.O. Edet, H. Louis, T.E. Gber, A.D. Nwagu, S.A. Adaliku, A. S. Adeyinka, Heteroatoms (B, N, and P) doped on nickel-doped graphene for phosgene (COCl<sub>2</sub>) adsorption: insight from theoretical calculations, *Mater. Today Sustain.* 21 (2023), 100294.
- [45] B.E. Inah, J.F. Eze, H. Louis, H.O. Edet, T.E. Gber, E.A. Eno, A.S. Adeyinka, Adsorption and gas-sensing investigation of oil dissolved gases onto nitrogen and sulfur doped graphene quantum dots, *Chem. Phys. Impact* 7 (2023), 100265.
- [46] D. Ma, J. Zhang, X. Li, C. He, Z. Lu, Z. Lu, Y. Wang, C<sub>3</sub>N monolayers as promising candidates for NO<sub>2</sub> sensors, *Sens. Actuators B* 266 (2018) 664–673.
- [47] S.G. Patel, A. González-Bakker, R.M. Vala, P.J. Patel, A. Puerta, A. Malik, H. M. Patel, Microwave-assisted multicomponent synthesis of antiproliferative 2, 4-dimethoxy-tetrahydropyrimido [4, 5-b] quinolin-6 (7 H)-ones, *RSC Adv.* 12 (47) (2022) 30404–30415.
- [48] R. Asapu, V.M. Palla, B. Wang, Z. Guo, R. Sadu, D.H. Chen, Phosphorus-doped titania nanotubes with enhanced photocatalytic activity, *J. Photochem. Photobiol. A* 225 (1) (2011) 81–87.
- [49] T.E. Gber, B. Etinwa, I. Benjamin, E. Ekereke, O.E. Offiong, A.S. Adeyinka, H. Louis, Functionalized boron doped graphene (BGP) as smart nanocarrier for delivery of hydroxyurea (HU) drug, *Chem. Phys. Impact* 7 (2023), 100291.
- [50] H. Roohi, N.A. Ardehijani, Adsorption performance of M-doped (M= Ti and Cr) gallium nitride nanosheets towards SO<sub>2</sub> and NO<sub>2</sub>: a DFT-D calculation, *RSC Adv.* 10 (46) (2020) 27805–27814.
- [51] A. Ahmadi, M. Kamfirooz, J. Beheshtian, N.L. Hadipour, The effect of surface curvature of aluminum nitride nanotubes on the adsorption of NH<sub>3</sub>, *Struct. Chem.* 22 (2011) 1261–1265.

- [52] A. Ahmadi, N.L. Hadipour, M. Kamfirooz, Z. Bagheri, Theoretical study of aluminum nitride nanotubes for chemical sensing of formaldehyde, *Sens. Actuators B* 161 (1) (2012) 1025–1029.
- [53] D.M. Patel, P.J. Patel, H.M. Patel, Catalytic stereoselective multicomponent reactions for the synthesis of spiro derivatives: recent progress, *Eur. J. Org. Chem.* 2022 (46) (2022), e202201119.
- [54] M.A. Akpe, H. Louis, T.E. Gber, C.M. Chima, O.I. Brown, A.S. Adeyinka, Modeling of Cu, Ag, and Au-decorated Al<sub>12</sub>Se<sub>12</sub> nanostructured as sensor materials for trapping of chlorpyrifos insecticide, *Comput. Theor. Chem.* 1226 (2023), 114218.
- [55] V. Magnasco, A. Perico, Uniform localization of atomic and molecular orbitals. I, *J. Chem. Phys.* 47 (3) (1967) 971–981.
- [56] T.C. Egemonye, H. Louis, T.O. Unimuke, T.E. Gber, H.O. Edet, V.M. Bassey, A. S. Adeyinka, Electronic structure theory investigation on the electrochemical properties of cyclohexanone derivatives as organic carbonyl-based cathode material for lithium-ion batteries, *Arab. J. Chem.* 15 (9) (2022), 104026.
- [57] J. Pipek, P.G. Mezey, A fast intrinsic localization procedure applicable for abinitio and semiempirical linear combination of atomic orbital wave functions, *J. Chem. Phys.* 90 (9) (1989) 4916–4926.
- [58] F.C. Asogwa, H. Louis, T.E. Gber, B.K. Isamura, S.A. Adalikwua, Electronic structure property and disposal efficiency of 2, 2-dichloropropionic acid using metalloids (B, Si, and Ge) decorated gallium nano-clusters (Ga<sub>12</sub>×12 (X= N, O)), *J. Comput. Biophys. Chem.* (2023). <https://doi.org/10.1142/S2737416523500515>.
- [59] P.M. Utsu, C.A. Anyama, T.E. Gber, A.A. Ayi, H. Louis, Modeling of transition metals coordination polymers of benzene tricarboxylate and pyridyl oxime-based ligands for application as antibacterial agents, *J. Indian Chem. Soc.* 100 (6) (2023), 100993.
- [60] P. Nkoe, A.L.E. Manicum, H. Louis, F.P. Malan, W.J. Nzondomyo, K. Chukwuemeka, T.O. Unimuke, Influence of solvation on the spectral, molecular structure, and antileukemic activity of 1-benzyl-3-hydroxy-2-methylpyridin-4 (1H)-one, *J. Mol. Liq.* 370 (2023), 121045.
- [61] E.I.I. Emmanuel, O.E. Duke, H. Louis, T.E. Gber, U.J. Undiandeye, A. Imojara, I. J. Ikot, Molecular Modeling of Cu (II), Zn (II), and Hg (II) Metal Complexes of (E)-Benzo [d][1, 3-dioxol-6-ylimino) methyl-4-bromophenol Schiffbase as Potential Antibacterial Agent, *Chem. Afr.* (2023) 1–18. <https://doi.org/10.1007/s42250-022-00575-2>.
- [62] H.O. Edet, H. Louis, U.C. Godwin, S.A. Adalikwu, E.C. Agwamba, A.S. Adeyinka, Single-metal (Cu, Ag, Au) encapsulated gallium nitride nanotube (Ga<sub>12</sub>NNT) as glucose nonenzymatic nanosensors for monitoring diabetes: perspective from DFT, visual study, and MD simulation, *J. Mol. Liq.* 384 (2023), 122209.
- [63] Z. Demircioğlu, Ç.A. Kaştaş, O. Büyükgüngör, Theoretical analysis (NBO, NPA, Mulliken population method) and molecular orbital studies (hardness, chemical potential, electrophilicity and Fukui function analysis) of (E)-2-((4-hydroxy-2-methylphenylimino) methyl)-3-methoxyphenol, *J. Mol. Struct.* 1091 (2015) 183–195.
- [64] Nicely L.G., Vala R.M., Upadhyay D.B., Nogales J., Chi C., Banerjee S., & Patel H.M. (2022). One-pot two-step catalytic synthesis of rationally designed 6-amino-2-pyridone-3, 5-dicarbonitriles enabling anti-cancer bioactivity.
- [65] D.M. Patel, H.J. Patel, J.M. Padrón, H.M. Patel, A novel substrate directed multicomponent reaction for the syntheses of tetrahydro-spiro [pyrazolo [4, 3-f] quinoline]-8, 5'-pyrimidines and tetrahydro-pyrazolo [4, 3-f] pyrimido [4, 5-b] quinolines via selective multiple C–C bond formation under metal-free conditions, *RSC Adv.* 10 (33) (2020) 19600–19609.
- [66] S.G. Patel, A. González-Bakker, R.M. Vala, P.J. Patel, A. Puerta, A. Malik, H. M. Patel, Microwave-assisted multicomponent synthesis of antiproliferative 2, 4-dimethoxy-tetrahydropyrimido [4, 5-b] quinolin-6 (7 H)-ones, *RSC Adv.* 12 (47) (2022) 30404–30415.
- [67] J. Martínez, Local reactivity descriptors from degenerate frontier molecular orbitals, *Chem. Phys. Lett.* 478 (4–6) (2009) 310–322.
- [68] U.J. Undiandeye, B.E. Inah, O.C. Godfrey, W. Emori, I. Anna, B.C. Okoro, H. Louis, Antilymphoma activities of benzo bithiazole derivative by molecular docking, impact of solvation, quantum chemical study, and spectroscopic (FT-IR, UV, NMR) investigation, *Chem. Phys. Impact* 7 (2023), 100290.
- [69] E.E. Okon, C. Osundu-Anyanwu, H.O. Edet, U.O. Edet, U.C. Godwin, A. Imojara, H. Louis, Spectral (FT-IR, NMR, UV) characterization, DFT studies, and molecular docking of hydrazine derivatives as antiviral agent for yellow fever (YFV), *J. Mol. Struct.* (2023), 136559.
- [70] A. Soltani, E. Tazikeh-Lemeski, M.B. Javan, A comparative theoretical study on the interaction of pure and carbon atom substituted boron nitride fullerenes with ifosfamide drug, *J. Mol. Liq.* 297 (2020), 111894.
- [71] D. Oche, H. Louis, V.M. Bassey, G.A. Okon, H.O. Edet, J.T. Jumbo, A.S. Adeyinka, First-principles study of adsorption and sensing properties of Re and Tc-doped gallium nitride nanotube (Ga<sub>12</sub>NNT) for oil-dissolved gases, *Results Chem.* 5 (2023), 100980.
- [72] P. Singla, M. Riyaz, S. Singhal, N. Goel, Theoretical study of adsorption of amino acids on graphene and BN sheet in gas and aqueous phase with empirical DFT dispersion correction, *Phys. Chem. Chem. Phys.* 18 (7) (2016) 5597–5604.
- [73] F.C. Asogwa, F.U. Eze, J.O. Mba, J.A. Ezugwu, H. Louis, T.E. Gber, D.I. Ugwu, Synthesis, vibrational analysis, electronic structure property investigation and molecular simulation of sulphonamide-based carboxamides against plasmodium species, *ChemistrySelect* 8 (5) (2023), e202203208.
- [74] H. Louis, T.E. Gber, D.E. Charlie, T.C. Egemonye, M.M. Orosun, Detection of hydroxymethanesulfonate (HMS) by transition metal-anchored fullerene nanoclusters, *J. Iran. Chem. Soc.* 20 (3) (2023) 713–729.
- [75] A. Bousseksou, G. Molnár, L. Salmon, W. Nicolazzi, Molecular spin crossover phenomenon: recent achievements and prospects, *Chem. Soc. Rev.* 40 (6) (2011) 3313–3335.
- [76] T.E. Gber, C.A. Agida, H. Louis, P.B. Ashishie, D. Oche, O.F. Ede, A.S. Adeyinka, Metals (B, Ni) encapsulation of graphene/PEDOT hybrid materials for gas sensing applications: a computational study, *Talanta Open* 8 (2023), 100252.
- [77] J. Garrido, A. Linares-Solano, J.M. Martín-Martínez, M. Molina-Sabio, F. Rodríguez-Reinoso, R. Torregrosa, Use of nitrogen vs. carbon dioxide in the characterization of activated carbons, *Langmuir* 3 (1) (1987) 76–81.
- [78] M.I. Ofem, C.A. Ayi, H. Louis, T.E. Gber, A.A. Ayi, Influence of anionic species on the molecular structure, nature of bonding, reactivity, and stability of ionic liquids-based on 1-butyl-3-methylimidazolium, *J. Mol. Liq.* 387 (2023), 122657.
- [79] E.L. Kechi, B.E. Inah, H.O. Edet, H. Louis, Studies on thiophene-thiazole-carbohydrazides as methicillin-resistant staphylococcus aureus (MRSA) agents: insight from DFT and Molecular docking simulation, *Chem. Phys. Impact* 7 (2023), 100271.
- [80] H.O. Edet, H. Louis, T.E. Gber, P.S. Idante, T.C. Egemonye, P.B. Ashishie, A. S. Adeyinka, Heteroatoms (B, N, S) doped quantum dots as potential drug delivery system for isoniazid drug: insight from DFT, NCI, and QAIM, *Heliyon* (2022) e12599.
- [81] H. Louis, I.O. Amodu, T.O. Unimuke, T.E. Gber, B.B. Isang, A.S. Adeyinka, Modeling of Ca<sub>12</sub>O<sub>12</sub>, Mg<sub>12</sub>O<sub>12</sub>, and Al<sub>12</sub>N<sub>12</sub> nanostructured materials as sensors for phosgene (Cl<sub>2</sub>CO), *Mater. Today Commun.* 32 (2022), 103946.
- [82] T.E. Gber, H. Louis, O.C. Ngana, I.O. Amodu, E.E. Ekereke, I. Benjamin, A. Adeyinka, Yttrium-and zirconium-decorated Mg<sub>12</sub>O<sub>12</sub>-X (X= Y, Zr) nanoclusters as sensors for diazomethane (CH<sub>2</sub>N<sub>2</sub>) gas, *RSC Adv.* 13 (36) (2023) 25391–25407.